Coupled fluid flow, solute transport and dissolution processes in discrete fracture networks: An advanced Discontinuous Galerkin model

Sara Tabrizinejadas, Anis Younes, Hussein Hoteit, Jerome Carrayrou, Marwan Fahs

Coupled fluid flow, solute transport and dissolution processes in discrete fracture networks: an advanced Discontinuous Galerkin model

Sara Tabrizinejadas[1], Anis Younes[2], Hussein Hoteit[3], Jerome Carrayrou[2], Marwan Fahs[2]*

[1]Universite de Pau et des Pays de l'Adour, E2S UPPA, CNRS, LMAP, Pau, France

[2] Institut Terre et Environnement de Strasbourg, Université de Strasbourg, CNRS, ENGEES, UMR 7063, 67084 Strasbourg, France

[3] Physical Science and Engineering Division, King Abdullah University of Science and Technology (KAUST), Thuwal, Saudi Arabia

Submitted to *Advances in Water Resources*

Contact author: Marwan Fahs

E-mail: fahs@unistra.fr

Abstract

Modeling dissolution processes in discrete fracture networks (DFNs) is a challenging task. Challenges are related to the highly nonlinear coupling between flow, mass transport, and reactive processes associated with fracture aperture evolution by dissolution. Further, advection-dominated transport due to fast fluid flow in fractures renders the problem more complex from a computational point of view, as traditional numerical methods may introduce unphysical oscillations or excessive numerical diffusion. The Discontinuous Galerkin (DG) method is known to be suitable for the simulation of advection-dominated transport. In this work, an advanced DG model is developed to model transport with dissolution in DFNs. We propose an upwind formulation to deal with the upstream concentration at the intersection of several fractures. The upstream concentration at an intersection node is calculated based on the average nodal concentrations of all the fractures having an inflow at that node, weighted by the volumetric fluxes of these fractures. The dispersion term is discretized with the Mixed Finite Element (MFE) method, which ensures the continuity of the dispersive flux at the intersection of fractures with different apertures. The obtained nonlinear coupled flow-transport-dissolution equations are discretized in time with a high-order scheme via the method of lines (MOL). Numerical examples and comparisons with standard finite element (FE) and finite volume (FV) solutions are performed to investigate the correctness and efficiency of the developed model. Results show that the new DG-DFN model avoids unphysical oscillations encountered with the standard FE method and strongly reduces the numerical diffusion observed with the upwind FV scheme. The DG-DFN model is then used to investigate the effect of the dissolution rate on the flow, transport, and aperture evolution processes for a single fracture and for a DFN. A quasi-linear evolution of the fracture aperture is observed for low dissolution rates. For high dissolution rates, a funnel-shaped enlargement is observed with a significant widening for the fractures near the inlet and minor effects for those away from the injection location.

Keywords: Dissolution processes; Fractured rocks; Discrete Fracture Network; Discontinuous Galerkin; advection-dominated transport.

1. Introduction

The flow of water in fractured rocks is usually associated with dissolution processes and transport of the dissolved species (Liu *et al.,* 2020). Naturally existing fractures as well as chemically-induced fractures can significantly affect the domain transmissivity that, in turn, affect flow, transport and dissolution processes. When the porosity and permeability of the rocks are low , the fractures act as preferential fluid pathways (Mukhametdinova et al., 2020). Therefore, fluid flow in the rock matrix can be neglected and therefore, the domain can be represented as a discrete fracture network (DFN) (Medici *et al.,* 2016, Lopes et al., 2022; Aliouache et al., 2019). Dissolution processes in DFNs are important in several environmental and engineering applications such as in heat extraction in geothermal reservoirs (Kim et al., 2015), recovery in oil reservoirs (Medekenova and Jones, 2014; Khoei et al. 2020; Sahu et al. 2023), radioactive and nuclear waste disposal (Graf and Therrien, 2007; Natarajan and Suresh Kumar, 2010) and carbon sequestration (Hosseini et al. 2020;Tran and Jha, 2021; Li et al. 2021).

Despite the wide range of applications, dissolution processes in DFNs are still poorly investigated (Lopes et al., 2022; Aliouache et al., 2019). Most of the existing studies have focused on dissolution processes in unfractured domains and how these processes can create preferential flow pathways (Hanna and Rajaram, 1998; Dijk et al., 2002; Detwiler et al., 2003; Detwiler and Rajaram, 2007; Deng and Spycher, 2019). Experimental investigations have shown that, depending on the experimental conditions, different dissolution behaviors can be observed. This complicates the interpretation of the effects of controlling parameters on the flow, transport, dissolution and fracture evolution processes (Detwiller and Rajaram, 2007). Modeling has been also used to understand fractures initiation and propagation in unfractured domains due to dissolution processes (Detwiler and Rajaram, 2007; Ameli *et al*., 2014; Deng and Spycher, 2019; Sahu et al. 2023). However, modeling-based studies for dissolution

processes in well-developed discrete fracture networks and the effect of the reaction rate on the dissolution of connected fractures are poorly investigated (Deng and Spycher, 2019).

Modeling dissolution processes in DFNs reveals specific challenges that are not present in unfractured media (Viswanathan et al., 2022). The main challenge is the dynamic evolution of the fractured system due to the geochemical dissolution (Tenthorey and Fitzgerald, 2006). The enlargement of fractures as a result of the dissolution process continuously affects the fluid flow, which in turn, affects the dissolution process and the transport of dissolved species. Therefore, the four processes (*i.e.* flow, transport, dissolution and fracture enlargement) are strongly coupled and nonlinear. In addition, in DFNs, the transport of the dissolved species is often advection-dominated due to fast fluid flow in fractures. In such a case, traditional numerical methods, such as standard finite element (FE) or finite volume (FV) methods can generate excessive numerical diffusion that may distort the dissolution process. Taditional numerical methods can also generate non-physical oscillations which can be the origin of convergence issues that hamper the applicability of the numerical models.

The Discontinuous Galerkin (DG) finite element method is well-adapted to capture sharp moving fronts occurring in advection-dominant transports (Younes and Ackerer, 2008). The discretization of the hyperbolic term of the transport equation with DG has been largely reported in the literature. For instance, Younes *et al*., (2014) have developed an efficient DG model for buoyancy-driven flow problems in unfractured porous media. In fractured domains, Zidane and Firoozabadi (2014) and Moortgat *et al.,* (2016) have developed a DG numerical model for multicomponent compressible flow in 2D and 3D domains. However, the developed schemes employed the DG method only for the transport in the matrix continuum. In these studies, transport in fractures, where advection is dominant, is modeled with an upwind first order FV scheme which is known to introduce excessive numerical diffusion (Konz *et al*., 2009). Recently, Younes et al. (2023) have used the DG method for modeling

coupled flow and mass transport processes in fractured porous media with no reactive processes and with constant fracture aperture. To the best of our knowledge, the DG method has never been used for modeling coupled flow, mass transport and reactive dissolution processes in a discrete fracture network.

The objective of this paper is to develop an advanced numerical model based on the DG method for the simulation of dissolution processes in DFNs, and to take advantage of this model for investigating the effects of geochemical dissolution rate on fracture evolution, flow and transport processes. The upwind P1-DG scheme developed by Younes *et al*. (2009) is adopted to simulate the advection processes in the network of 1D fractures. With this scheme, the degrees of freedom are the mean concentration on elements and the concentration gradient. The Riemann solver is then used to evaluate the concentration at the nodes. The main challenge in applying this technique for a DFN is the evaluation of the concentration at nodes of intersection of several fractures. A new formulation is developed in this work where the upstream concentration at a fracture intersection node is calculated using the average of the concentrations of all fractures providing flow to that node, weighted by the flow rate in the corresponding fractures.

Darcy's law combined with the cubic law is used to simulate flow within the fractures. The flow equations are discretized with the hybrid formulation of the Mixed Finite Element (MFE) method (Younes *et al*., 2009). The mass lumping technique developed by Koohbor *et al*. (2020) is employed to avoid over- and under-shoots observed in transient flow simulations with small time steps. The MFE method is also used for the discretization of the dispersion term to ensure the continuity of the dispersive flux at nodes where several fractures with different apertures intersect. The highly nonlinear coupled equations of fluid flow, advection-dispersion transport and aperture evolution due to dissolution are solved simultaneously in order to avoid operator-splitting errors. The time discretization is performed using a high

order integration method via the method of lines (MOL). MOL has been demonstrated to be very efficient in solving high nonlinear systems of equations, such as unsaturated flow in porous media (Fahs et al., 2009; Farthing et al., 2003; Miller et al., 2006). With MOL, the spatial derivatives are discretized while the time derivatives are kept in their continuous form. This allows for converting the partial differential equations to a system of ordinary differential equations. Then, we use high order implicit time discretization with the DASPK solver (Brown et al., 1994) which is highly efficient and accurate for solving nonlinear systems with a large number of unknowns (Younes *et al*., 2011).

The paper is organized as follows: First, the partial differential equations describing flow, transport and dissolution processes are presented. Second, the new DG-DFN numerical model is described. Then, the validation and accuracy of the new model is investigated by comparison against a standard FE model, obtained using COMSOL Multiphysics, and an in-house upwind FV model. Finally, the DG model is employed to investigate the effect of the dissolution rate on flow, transport and aperture evolution for a single fracture and for a DFN.

2. The Mathematical model

The fractures are simulated as highly permeable porous media. The permeability of the fractures is estimated using the well-known Poiseuille equation (Hanna and Rajaram, 1998). The flow process in a fracture with a variable aperture $b[L]$ is governed by the fluid mass conservation equation:

$$\frac{\partial(\theta b)}{\partial t} + \nabla.(b\boldsymbol{q}) = 0 \tag{1}$$

and the Darcy law:

$$\boldsymbol{q} = -\frac{\rho_0 g\,\kappa}{\mu}\nabla H = -\frac{\rho_0 g b^2}{12\mu}\nabla H \tag{2}$$

where, $H[L]$ is the hydraulic head, $t[T]$ is the time and $\boldsymbol{q}\left[L.T^{-1}\right]$ is the Darcy velocity, $b[L]$ is the local fracture aperture, $\theta[-]$ is the porosity, $g\left[L.T^{-2}\right]$ is the gravity acceleration, $\mu\left[M.L^{-1}.T^{-1}\right]$ is the dynamic viscosity of the fluid and $\kappa\left[L^2\right]$ is the permeability calculated using the cubic law $\kappa = \frac{b^2}{12}$ (Witherspoon *et al.*, 1980; Graf and Therrien, 2007; He *et al.*, 2021).

Under isothermal conditions and no precipitation processes, the mass conservation of a contaminant species through a fracture, taking into account the dissolution process, is ruled by the advection-dispersion-reaction equation (Detwiler and Rajaram, 2007):

$$\frac{\partial(\theta bC)}{\partial t} + \nabla.(b\boldsymbol{q}C) - \nabla.(b\boldsymbol{D}\nabla C) = R(C) \tag{3}$$

where, $C\left[M.L^{-3}\right]$ is the concentration of the dissolved species, $R(C)\left[M.L^{-2}.T^{-1}\right]$ is the reaction term and $\boldsymbol{D}\left[L^2.T^{-1}\right]$ is the velocity-dependent dispersion tensor for a fracture filled by a porous medium.

The transport Eq. (3) writes

$$\theta b\frac{\partial C}{\partial t} + C\left(\frac{\partial(\theta b)}{\partial t} + \nabla.(b\boldsymbol{q})\right) + b\boldsymbol{q}.\nabla C - \nabla.(b\boldsymbol{D}\nabla C) = R(C) \tag{4}$$

which, using Eq. (1), simplifies to

$$\theta b\frac{\partial C}{\partial t} + b\boldsymbol{q}.\nabla C - \nabla.(b\boldsymbol{D}\nabla C) = R(C) \tag{5}$$

In the case of one-dimensional fracture, D is given by:

$$D = \alpha_L \times |\boldsymbol{q}| + D_m \tag{6}$$

where, $\alpha_L[L]$ is the longitudinal dispersivity in the fracture and $D_m\left[L^2.T^{-1}\right]$ is the diffusion coefficient of the dissolved species.

Due to dissolution, the fracture aperture evolves during time as follows:

$$\rho_r \times \delta \times \frac{\partial b}{\partial t} - R(C) = 0 \tag{7}$$

where $\rho_r\left[M.L^{-3}\right]$ is the density of the rock and $\delta[-]$ is a stoichiometric coefficient that represents the mass of mineral entering solution for a unit mass of dissolved rock.

In this work, under the assumption of no precipitation processes, the reaction term $R(C)$ representing the dissoulution processes is modeled using a first-order approximation with a constant reaction rate (Hanna and Rajaram, 1998; Detwiler and Rajaram, 2007; Steefel and Lasaga, 1994; Steefel and Lichtner, 1998):

$$R(C) = K_C\left(C_S - C\right) \tag{8}$$

where, $K_C\left[L.T^{-1}\right]$ is the constant reaction rate and $C_S\left[M.L^{-3}\right]$ is the concentration of the contaminant species at saturation.

3. The numerical model

To solve the set of equations (1-8) for flow, transport, and aperture evolution, we selected numerical methods that provide accurate and consistent solutions for each kind of equation. Thereby, the spatial discretization is based on the combination of the MFE method for flow and dispersion, the upwind DG method for advection, and the FV method for reaction. We summarize the main steps of the spatial discretization that allows for obtaining a system of coupled ordinary differential equations. This system is then solved with the DASPK time integration solver. The notations used for the spatial discretization of the flow and transport

are shown in Figure 1. In this figure NC_i (resp. NH_i) represents the concentration (resp. hydraulic head) at the intersection node i. TC^k (resp. TH^k) represents the concentration (resp. hydraulic head) at the fracture k. q_i^k is the outlet water flux at the node i of the fracture k.

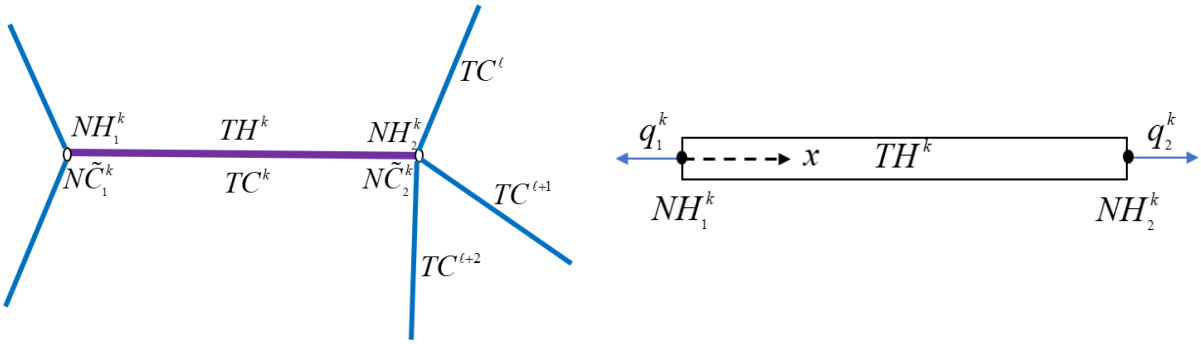

Figure 1. Flow and transport notations in a fracture k.

3.1 Spatial discretization of the flow

The flow in the fracture network is discretized with the MFE method. Thus, for a fracture k of length ℓ^k and width b^k, the velocity is approximated with linear test functions as follows:

$$q^k = \sum_{j=1}^{2} q_j^k w_j^k \tag{9}$$

where, q^k is the velocity inside the fracture k, $w_1^k = \dfrac{x-\ell^k}{b^k \ell^k}$ and $w_2^k = \dfrac{x}{b^k \ell^k}$ are the linear interpolation functions of the MFE method and q_j^k is the flux leaving the node j of the fracture k.

The continuity Eq. (1) is integrated over the fracture k yielding the following mass conservation equation:

$$\theta^k \ell^k \frac{\partial b^k}{\partial t} + q_1^k + q_2^k = 0 \tag{10}$$

The variational formulation of Darcy's law Eq. (2) using w_i^k as a test function gives:

$$\sum_{j=1}^{2} q_j^k \int_0^{\ell^k} w_i^k w_j^k = -\frac{\rho_0 g\left(b^k\right)^2}{12\mu} \int_0^{\ell^k} \nabla H w_i^k \tag{11}$$

Integration by part leads to:

$$\sum_{j=1}^{2} q_j^k \int_0^{\ell^k} w_i^k w_j^k = -\frac{\rho_0 g\left(b^k\right)^2}{12\mu} \left(\int_0^{\ell^k} H\left(\nabla w_i^k\right) - \left[H w_i^k \right]_{x=0}^{x=\ell^k} \right) \tag{12}$$

Using the trapezoidal rule for the evaluation of the left integral yields:

$$q_i^k = \frac{\rho_0 g\left(b^k\right)^2}{12\mu} \times \frac{2b^k}{\ell^k} \left(TH^k - NH_i^k \right) \tag{13}$$

Eq. (13)is then substituted into Eq. (10) to obtain:

$$-\theta^k \ell^k \frac{\partial b^k}{\partial t} + \frac{\rho_0 g\left(b^k\right)^3}{6\ell^k \mu} \left(NH_1^k + NH_2^k - 2TH^k \right) = 0 \tag{14}$$

To close system (14), mass conservation is written at each node of fracture intersection. At the node i surrounded by n fractures, we have:

$$\sum_n q_i^n = Q_i^* \tag{15}$$

where Q_i^* is the pumped/injected quantity at the intersection node *i*.

Substituting Eq. (13) into Eq. (15) yields:

$$\sum_n \frac{\rho_0 g\left(b^n\right)^3}{6\ell^n \mu} \left(TH^n - NH_i^n \right) = Q_i^* \tag{16}$$

Hence, the head NH_i at the intersection node *i* writes

$$NH_i = \frac{\sum_n \left(\frac{\rho_0 g \left(b^n\right)^3}{6\ell^n \mu} TH^n \right) - Q_i^*}{\sum_n \frac{\rho_0 g \left(b^n\right)^3}{6\ell^n \mu}} \tag{17}$$

For a given fracture network, the flow system is formed by writing Eq. (14) for all the fractures k in which, NH_1^k and NH_2^k are substituted using Eq. (17). This system is solved for the head traces TH^k at all mesh edges. Hence, the flow system has the number of fracture cells as degrees of freedom (DOF).

3.2 Spatial discretization of the transport

The DG method, which is well adapted for transport with sharp interface fronts, is employed for the discretization of the advection equation. With this method, we assume a linear discontinuous approximation of the concentration:

$$C^k(x,t)|_k = \phi_1^k(x) \times TC^k + \phi_2^k(x) \times C_x^k \tag{18}$$

where C^k is the concentration at the fracture k, which has two degrees of freedom: TC^k and C_x^k. TC^k is the average value of concentration in the fracture k and C_x^k is the concentration variation along the fracture direction. The corresponding interpolation functions are:

$$\phi_1^k(x) = 1, \qquad \phi_2^k(x) = x - \bar{x}_k \tag{19}$$

where $\bar{x}_k$ is the center of the fracture k.

The weak formulation of the transport Eq. (5) writes:

$$\theta^k b^k \int_0^{\ell^k} \frac{\partial C}{\partial t} \phi_i + b^k \int_0^{\ell^k} \nabla.(\boldsymbol{q} C \phi_i) - b^k \int_0^{\ell^k} C \phi_i \nabla.\boldsymbol{q} - b^k \int_0^{\ell^k} C \boldsymbol{q} \nabla \phi_i - \int_0^{\ell^k} \nabla.(b\boldsymbol{D}\nabla C)\phi_i = \int_0^{\ell^k} R(C)\phi_i \tag{20}$$

In the following, we develop the calculation of the second term, for which a specific treatment is developed to solve the Riemann problem, and the fifth dispersive term, which is calculated

with the MFE to ensure the continuity of the dispersive flux at the intersection of several fractures.

The second term is transformed into a boundary integral where the Riemann problem is solved at the interface as follows:

$$b^k \int_0^{\ell^k} \nabla.\left(\boldsymbol{q} C \phi_i\right) = b^k \left(q_1^k C_1^{k,*} \phi_i \big|_{x=0} + q_2^k C_2^{k,*} \phi_i \big|_{x=\ell^k} \right) \tag{21}$$

The upstream concentration $C_j^{k,*}$ is given by

$$\left(C_j^{k,*}\right)_{j=1,2} = \begin{cases} NC_{j,in}^k & if \quad q_j^k \geq 0 \\ NC_{j,out}^k & if \quad q_j^k < 0 \end{cases} \tag{22}$$

where, $NC_{j,in}^k$ and $NC_{j,out}^k$ are the interior and outer concentrations at the node j of the fracture k, respectively.

The interior concentration $NC_{j,in}^k$ at the node j is obtained from Eq. (18):

$$NC_{j,in}^k = TC^k + \tau_j^k C_x^k \tag{23}$$

with $\tau_1^k = -\frac{\ell^k}{2}$ corresponding to the first node and $\tau_2^k = \frac{\ell^k}{2}$ to the second node of k.

The concentration $NC_{j,out}^k$ is calculated using the interior concentration $\left(NC_{j,in}^n\right)$ of all the fractures n sharing the node j and having a positive flux q_j^n as follows:

$$NC_{j,out}^k = \left. \frac{\sum_n q_j^n NC_{j,in}^n}{\sum_n q_j^n} \right|_{q_j^n \geq 0} \tag{24}$$

Thus, the second integral in Eq. (20) can be written in the following form:

$$b^k \int_0^{\ell^k} \nabla.\left(\boldsymbol{q} C \phi_i\right) = b^k q_1^k \begin{bmatrix} \varepsilon_1^k & \left(1-\varepsilon_1^k\right) \\ \varepsilon_1^k \tau_1^k & \left(1-\varepsilon_1^k\right)\tau_1^k \end{bmatrix} \begin{bmatrix} NC_{1,in}^k \\ NC_{1,out}^k \end{bmatrix} + b^k q_2^k \begin{bmatrix} \varepsilon_2^k & \left(1-\varepsilon_2^k\right) \\ \varepsilon_2^k \tau_2^k & \left(1-\varepsilon_2^k\right)\tau_2^k \end{bmatrix} \begin{bmatrix} NC_{2,in}^k \\ NC_{2,out}^k \end{bmatrix} \quad (25)$$

where ε_j^k is such that $\varepsilon_j^k = 1$ if $q_j^k \geq 0$, else $\varepsilon_j^k = 0$.

Using the MFE approximation for the dispersive flux $\tilde{q} = -D\nabla C$, the fifth dispersive integral in Eq. (20) writes:

$$-\int_0^{\ell^k} \nabla.\left(bD\nabla C\right)\phi_i = \int_0^{\ell^k} \nabla.\left(b\tilde{q}\right)\phi_i = \frac{\tilde{q}_1^k + \tilde{q}_2^k}{\ell^k} \int_0^{\ell^k} \phi_i = \begin{bmatrix} \left(\tilde{q}_1^k + \tilde{q}_2^k\right) \\ 0 \end{bmatrix} \quad (26)$$

where, $\tilde{q}_j^k$ is the dispersive flux at the node j of the fracture k, calculated in a similar manner to the Darcy flux Eq. (13):

$$\tilde{q}_j^k = b^k D_k \frac{TC^k - N\tilde{C}_j}{\ell^k / 2} \quad (27)$$

where $N\tilde{C}_j$ is the concentration at the node j.

$N\tilde{C}_j$ is calculated by imposing the continuity of the dispersive flux of all the fractures (including k) sharing the node j. For a node j shared by n fractures, $N\tilde{C}_j$ is such that:

$$\sum_n 2b^n D_n \frac{TC^n - N\tilde{C}_j}{\ell^n} = 0 \quad (28)$$

which yields:

$$N\tilde{C}_j = \frac{\sum_n \frac{b^n}{\ell^n} D_n TC^n}{\sum_n \frac{b^n}{\ell^n} D_n} \quad (29)$$

Thus, Eq. (27) becomes:

$$\tilde{q}_j = 2\frac{b^k}{\ell^k} D_k \left(TC^k - \frac{\sum_n \frac{b^n}{\ell^n} D_n TC^n}{\sum_n \frac{b^n}{\ell^n} D_n} \right) \tag{30}$$

If the fracture k is filled by a porous medium, the dispersion coefficient is approximated by:

$$D_k = \alpha_L^k \left| \bar{q}_k \right| + D_m \tag{31}$$

where, α_L^k is the longitudinal dispersivity through the fracture k and $\bar{q}_k = \frac{\left(q_2^k - q_1^k\right)}{2b_k}$ is the mean Darcy velocity in k.

Finally, the calculation of all integrals of the transport Eq. (20) gives

$$\begin{aligned} &\left[M_1\right]\begin{bmatrix} \frac{\partial TC^k}{\partial t} \\ \frac{\partial C_x^k}{\partial t} \end{bmatrix} + b^k q_1^k \begin{bmatrix} \varepsilon_1^k & \left(1-\varepsilon_1^k\right) \\ \varepsilon_1^k \tau_1^k & \left(1-\varepsilon_1^k\right)\tau_1^k \end{bmatrix} \begin{bmatrix} NC_{1,in}^k \\ NC_{1,out}^k \end{bmatrix} + \\ &b^k q_2^k \begin{bmatrix} \varepsilon_2^k & \left(1-\varepsilon_2^k\right) \\ \varepsilon_2^k \tau_2^k & \left(1-\varepsilon_2^k\right)\tau_2^k \end{bmatrix} \begin{bmatrix} NC_{2,in}^k \\ NC_{2,out}^k \end{bmatrix} + \left[M_2\right] \begin{bmatrix} TC^k \\ C_x^k \end{bmatrix} + \begin{bmatrix} \left(\tilde{q}_1^k + \tilde{q}_2^k\right) \\ 0 \end{bmatrix} = \begin{bmatrix} \ell^k R\left(TC^k\right) \\ 0 \end{bmatrix} \end{aligned} \tag{32}$$

where the terms of the (2×2) local matrices are $M_{1,ij} = \theta^k b^k \int_0^{\ell^k} \phi_i^k \phi_j^k$ and $M_{2,ij} = -\left(q_1^k + q_2^k\right)\int_0^{\ell^k} \phi_i^k \phi_j^k - b^k \int_0^{\ell^k} \phi_j^k \, \boldsymbol{q} \nabla \phi_i^k$, the expressions of $NC_{1,in}^k$ and $NC_{1,out}^k$ are given by Eq. (23) and Eq. (24) and the dispersive fluxes $\tilde{q}_1^k$ and $\tilde{q}_2^k$ are given by Eq. (30).

If dissolution is considered, the aperture of the fracture can evolve with time, as ruled by Eq. (7). The integration of this equation on the fracture k gives

$$\rho_r \delta \frac{\partial b^k}{\partial t} \ell^k - \ell^k R\left(TC^k\right) = 0 \tag{33}$$

Plugging Eq. (8) into Eq. (33) yields

$$\rho_r \delta \frac{\partial b^k}{\partial t} - K_C \left(C_S - TC^k \right) = 0 \tag{34}$$

The final coupled nonlinear flow-transport-dissolution system to solve is formed by: (*i*) the flow Eq. (14) in which we substitute Eq. (17) yielding the hydraulic head at the fracture cells of the DFN, (*ii*) the transport Eqs. (23), (24), (30) and (32), which yield the mean and the variation of the concentration in each fracture and the (*iii*) the dissolution Eq. (34), which gives the aperture for each fracture.

The obtained nonlinear system is discretized in time, via the method of lines. The main idea of this method is to keep the time derivative in its continuous form and to discretize the space derivatives. This results in a system of ODEs. The ODE system is solved using the DASPK solver which is based on a higher time integration scheme (Backward differentiation formula or Adams method). The resulting nonlinear system is solved using the Newton-Raphson method. The linear system arising at each time step is solved with the preconditioned Krylov iterative method. The solver adapts both the time step size and the order of the time integration scheme in order to reach the prescribed accuracy. Time step and order of integration are updated based on error control. In this work the accuracy is prescribed with a relative tolerance of 10^{-6}. Details of the MOL and the use of DASPK for nonlinear coupled flow transport systems are given in Younes *et al*. (2011; 2022).

4. Accuracy of the DG-DFN model

This section aims at verifying the correctness of the developed DG-DFN model and evaluating its performance for the simulation of advection dominant transport with dissolution in a fracture network. To this aim, the results of the DG-DFN model are compared to the results of COMSOL Multiphysics, which is based on the standard FE method, and to an in-house upwind FV model. Three examples are investigated. The two first examples deal

respectively with dispersion dominant and advection dominant linear transport in a DFN. The third example deals with coupled flow, transport, and aperture fracture evolution due to dissolution in a single fracture with high diffusion.

4.1 Transport with high dispersion in a DFN (example 1)

Analytical solutions are often of great interest for the verification of numerical codes. For coupled flow, transport and dissolution processes, some analytical and reference solutions were developed under simplified conditions (Hayek *et al.,* 2012; Suk 2016). However, these solutions cannot deal with fractured domains. Verification in fractured domains cannot be performed against analytical solution. Therefore, to verify our newly developed code, we use a standard FE numerical model developed in COMSOL Multiphysics software and an in-house model based on the upwind FV method. The generation of the stochastic network is performed with the "Discrete Fracture Network Add-In" which is available in the recent versions of COMSOL. This Add-In creates a randomized distribution of position, size, orientation and aperture for the fracture network. We used power law stochastic rule to create the network as in Barton and Zoback (1992) and Hooker *et al.,* (2009). The network of fracture for the Example 1 is shown in Figure 2a. A constant head gradient is imposed on the network from left to right. The horizontal domain is initially free of contaminant. The left inlet boundary of the domain has a fixed concentration. An outflow boundary condition is considered for the right side of the domain. Impermeable boundary conditions are considered on the top and bottom boundaries. The parameters for Example 1 are given in Table 1. This first example involves high values of dispersion and diffusion to avoid unphysical oscillations.

The results of the numerical models are compared on two observation points (O_1 and O_2) and for a monitoring fracture (F_1) which is highlighted in Figure 2b.

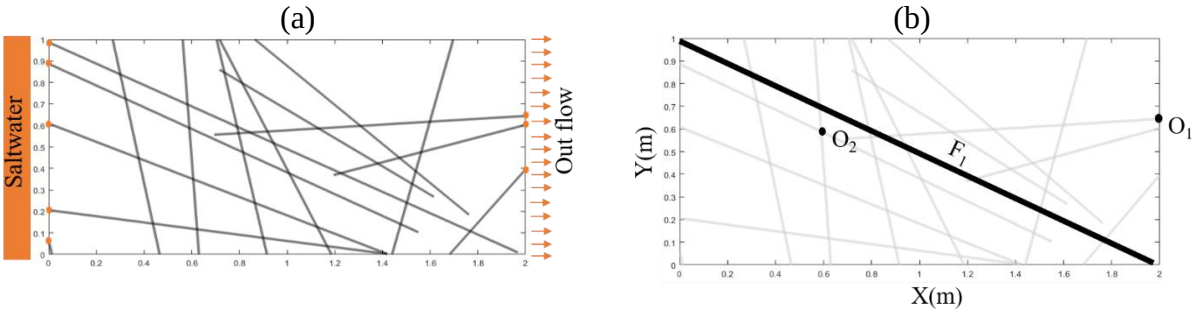

Figure 2. Problem description: (a) fracture network and boundary conditions, (b) Highlighted observation points (O_1, O_2), and a monitoring fracture (F_1)

Table 1: Parameters used in the three test examples.

Freshwater density	$\rho_0 = 1000$ kg.m^{-3}		
Porosity	1.0		
Viscosity	$\mu = 0.001$ Pa.s		
Rock density	$\rho_r = 27000$ mol/m^3		
Stoichiometric coefficient	$\delta = 0.4$ kg/m^3		
	Example 1	Example 2	Example 3
Diffusion	$D_m = 10^{-6}$ m^2/s	$D_m = 10^{-9}$ m^2/s	$D_m = 10^{-7}$ m^2/s
Dispersivity	$\alpha = 0.2$ m	$\alpha = 0$	$\alpha = 0$
Initial Thickness	$b = 1$cm	$b = 1$cm	$b_0 = 1$mm
Permeability	$\kappa = 10^{-11}$ m^2	$\kappa = 10^{-9}$ m^2	$\kappa = b^2/12$
Head at the upstream	$H_1 = 1$m	$H_1 = 1$m	$H_1 = 0.01$m
Head at the downstream	$H_0 = 0$	$H_0 = 0$	$H_0 = 0$
Reaction rate	$(-)$	$(-)$	$K_C = 10^{-5}$ m/s
Initial concentration	$C_0 = 0$	$C_0 = 0$	$C_0 = 0.1768$ mol/m^3
Inlet concentration	$C_{inj} = 35$ g/l	$C_{inj} = 35$ g/l	$C_{inj} = 0$

The distribution of dimensionless concentration in the fracture network after 14 hours with DG and FE models are shown in Figures 3a and 3b, respectively. The dimensionless concentration is calculated as the ratio of the concentration to the concentration of injected fluid. Similar concentration distributions are obtained with DG and FE solutions. The evolution of the concentration with time with DG, FE and FV methods at the two observation points O_1 and O_2 are depicted in Figures 3c and 3d, respectively. The concentration with the

three models after 14 hours along F_1 are also plotted in Figure 3e. Excellent agreement is observed between the three model solutions (Figures 3c-3e). These figures show the correctness of the newly developed DG-DFN model.

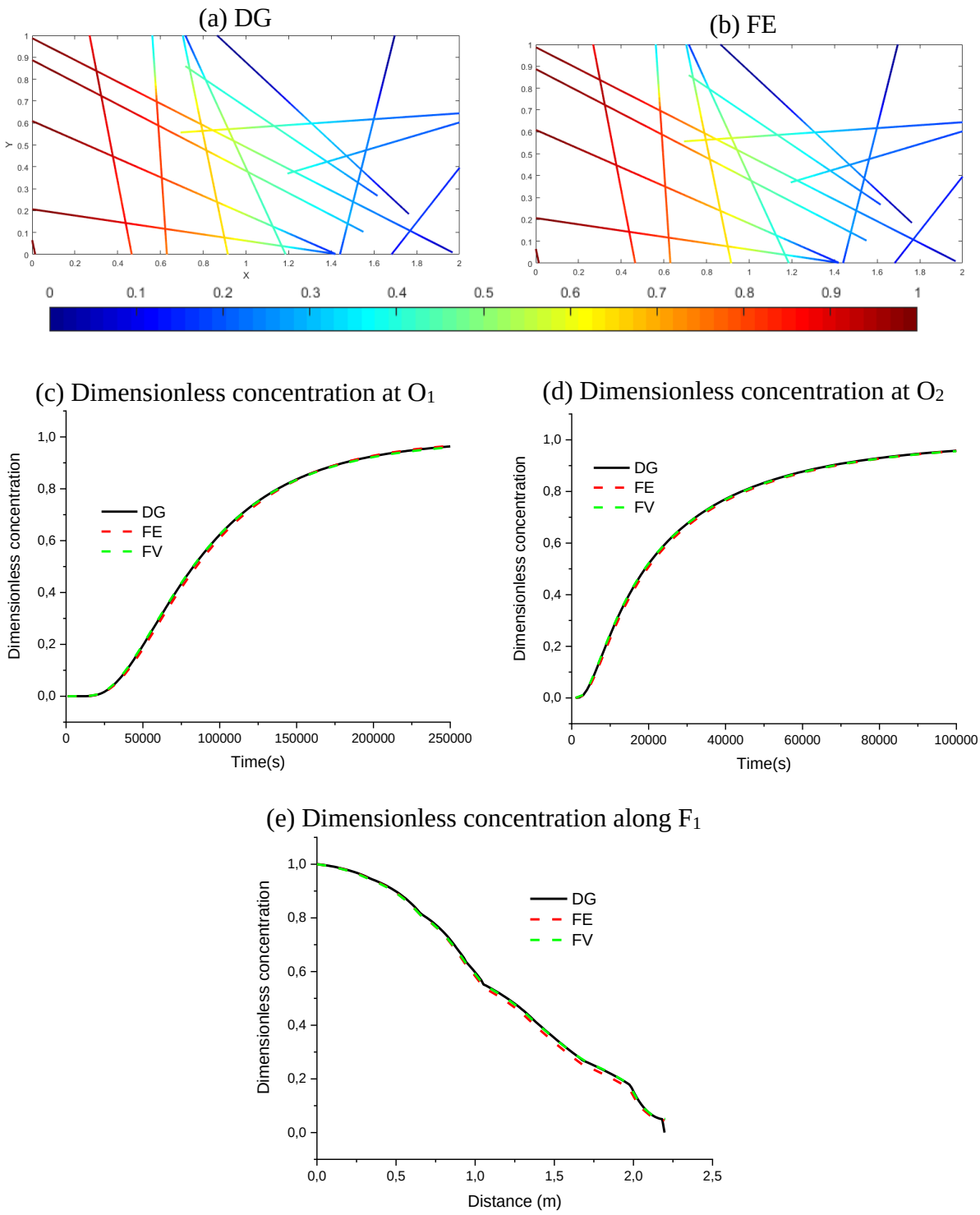

Figure 3. Results for Example 1: distributions of the dimensionless concentration with DG (a) and FE (b) methods. Time variation of the concentrations at O_1 (c), at O_2 (d) and concentration distribution along the fracture F_1 (e) with the DG, FV and FE methods.

4.2 Advection-dominated transport in a DFN (Example 2)

This example aims at investigating the advantages of the developed DG-DFN model in the case where the transport is advection dominated because of the fast fluid flow inside the fractures. The example is similar to Example 1, but we assume very little diffusion and no dispersion. The input parameters for Example 2 are given in Table 1.

A mesh sensitivity analysis is performed with the DG, FV and FE methods. It is observed that with the DG scheme, a mesh-independent solution is obtained with a relatively coarse mesh (272 nodes). The time variation of concentration at the observation point O_2 obtained with DG using a coarse mesh formed by 272 nodes is compared to the solution of FE and FV using two meshes: a coarse mesh formed by 272 nodes and a fine mesh formed by 1145 nodes. The results of FE on the coarse mesh show strong unphysical oscillations (note plotted). When the mesh is refined, the FE solution improves but still contains important unphysical oscillations in the vicinity of the sharp concentration fronts (Figure 4a). The FV solution with the coarse mesh shows large numerical diffusion smearing the concentration front. When the mesh is refined, the FV solution yields smaller numerical diffusion and the FV results converge toward the DG results.

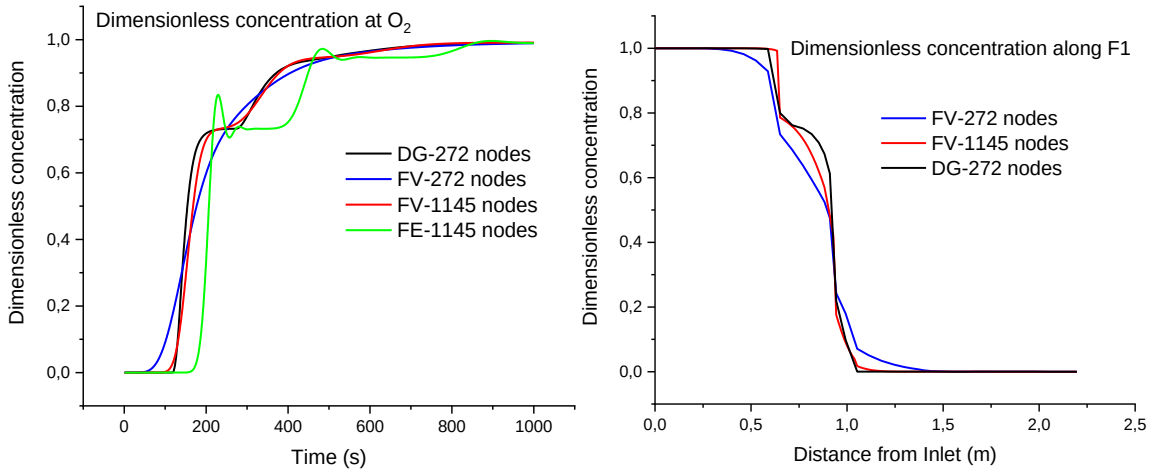

Figure 4. Comparison between DG, FE and FV for Example 2: (a) Time variation of the dimensionless concentration at the observation point O_2 and (b) distribution of the dimensionaless concentration at t=200s along line F_1.

The convergence of FV results toward DG results by refining the mesh is also observed in the concentration profile along F_1 which is plotted at the time t=200 seconds in Figure 4b. This figure shows that the FV concentration profile along line F_1 is spread when using 272 nodes due to numerical diffusion. The use of a mesh formed by 1145 nodes improves the FV results, although they remain less accurate than the DG results with only 272 nodes. These results confirm the high accuracy and efficiency of the DG model for advection dominant transport in DFNs since it avoids the unphysical oscillations observed with FE and the large numerical diffusion observed with FV.

4.3 Coupled flow, transport and dissolution in a single fracture with high diffusion (Example 3)

The simulated examples 1 and 2 allowed for the verification of the new DG code in the case of flow and transport in fractures with constant apertures (i.e., without dissolution). However, one of the challenges of the DG-DFN model is the accurate simulation of coupled flow-transport-dissolution processes with fracture evolution. Simulating these processes in a DFN is not possible with COMSOL. Hence, in this example, we consider flow and transport in a variable aperture single fracture (Figure 5). The fracture of 1m length is initially saturated by

the dissolving species. Freshwater is injected into the fracture from the left boundary and leaves from the right. The COMSOL model has been developed by using 1D geometry and coupling the interfaces 'Darcy's Law –*dl*' for flow and 'Transport of Diluted Species in Porous media –*tds*' for transport. Reaction term has been included in the transport with the module "Reaction". Equation (7) describing the evaluation of the fracture aperture due to dissolution processes is considered in COMSOL using the interface "Domain ODEs and DAEs" with the module "Distributed ODE". All the equations are solved simultaneously in COMSOL with the fully coupled approach.

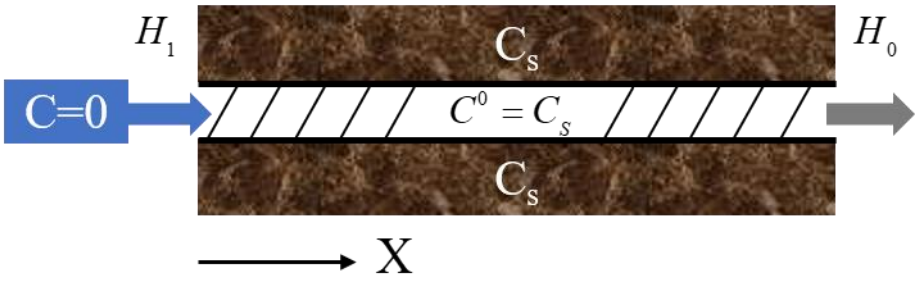

Figure 5. Conceptual model for dissolution in a single fracture.

The input parameters for Example 3 are shown in Table 1. The head difference $\Delta H = 0.01\text{m}$ corresponds to an initial velocity of 0.00833 m/s (720 m/day). The problem is simulated with a high diffusion value $D_m = 10^{-7}$ $\text{m}^2.\text{s}^{-1}$. This high value enables a fair comparison between the FE, FV and DG models since it allows reducing the unphysical oscillations observed with the FE solution and the numerical diffusion generated by the upwind FV scheme. The three numerical models (FE, FV and DG) are employed to calculate the concentration of the solute species in the domain as well as the evolution of the thickness of the fracture due to the dissolution process. The temporal and spatial variation of the dimensionless concentration and of the fracture thickness are plotted in Figure 6. The dimensionless concentration is calculated as the ratio of the concentration to the initial concentration in the domain.

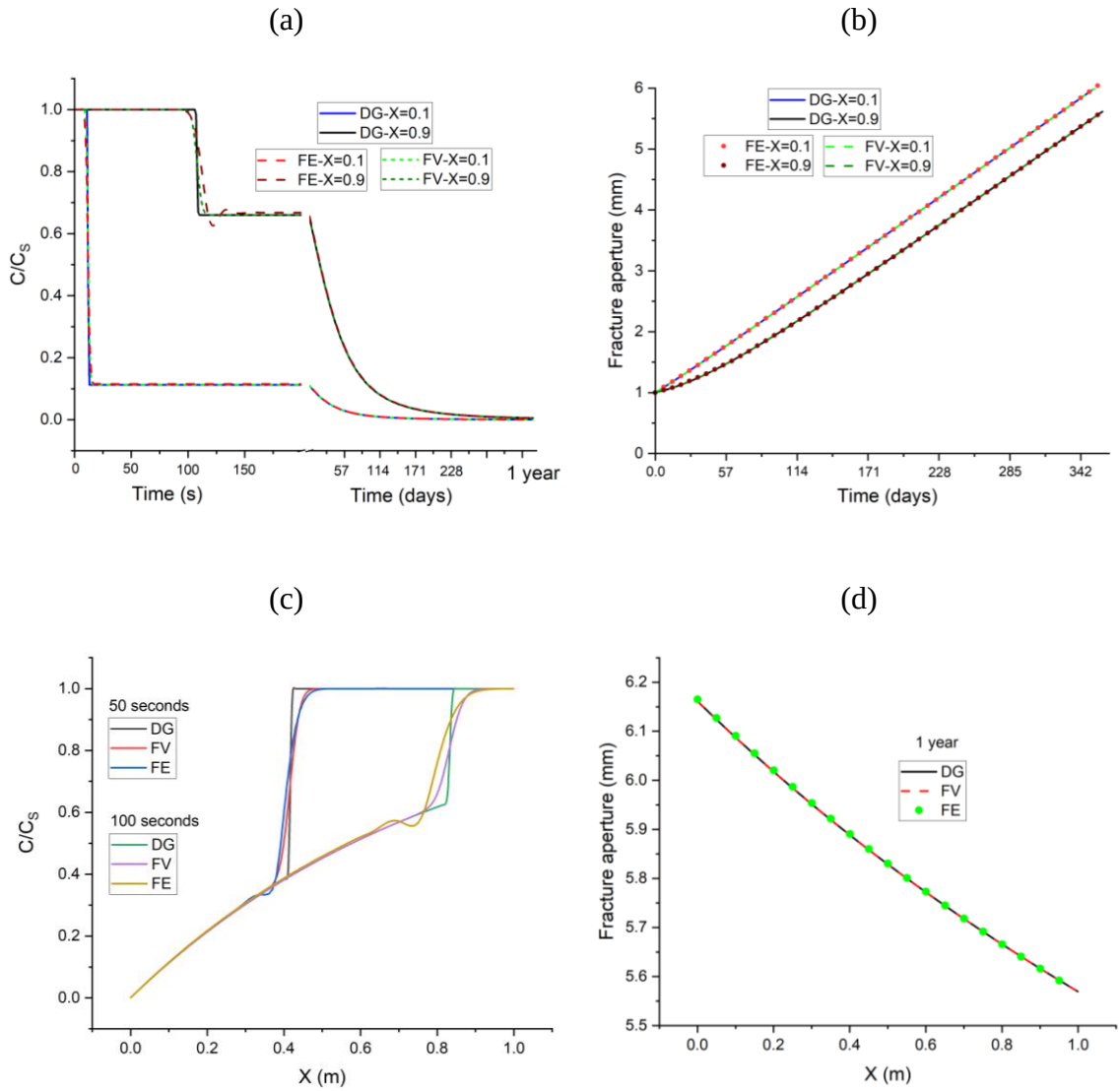

Figure 6. Example 3: Comparison between the FE, FV and DG results for dissolution in a single fracture: (a) time variation of the dimensionless concentration, (b) time variation of fracture aperture, (c) distributoin of the dimesnsionless concentration along the fracture after 50 and 100 seconds and (d) aperture of the fracture after one year.

Figures 6a and 6b show the time variation of the dimensionless concentration as well as the thickness at two different points of the domain (x=0.1m and 0.9m). The dimensionless concentration at t=50s and 100s and the thickness after one year are also plotted along the fracture in Figures 6c and 6d, respectively. Although we have used a high diffusion value, the results show numerical oscillations in the FE solution, especially near the outlet (Figures 6a and 6c). These oscillations are notably observed at short times and disappear in the mid and

long-term results. Indeed, in short times, advection is the dominant process that derives the freshwater/saltwater front towards the outlet. At long times, dissolution and diffusion become significant processes affecting thickness and concentration evolutions. Despite the differences observed between the short-time concentrations of the three schemes, the long-term results are almost similar, and the three numerical models yield equivalent results for the concentration distribution and the aperture evolution. These results show the correctness of the DG-DFN model for coupled flow-transport-dissolutions problems.

5. Effect of the dissolution rate on the flow, transport and aperture evolution

In this section, the DG-DFN model is used to investigate the effect of the dissolution rate on the flow, transport and aperture evolution in the case of a single fracture and in the case of a DFN.

4.1 The case of a single fracture

The investigated test case is similar to Example 3 (Figure 5), but we consider a more realistic problem with a reduced diffusion coefficient $D_m = 10^{-9}$ m^2.s^{-1} and use the new DG model to assess the effect of the dissolution rate on the fracture aperture evolution. The problem is simulated using low ($K_C = 10^{-5}$ m/s) and high ($K_C = 10^{-4}$ m/s) dissolution rates.

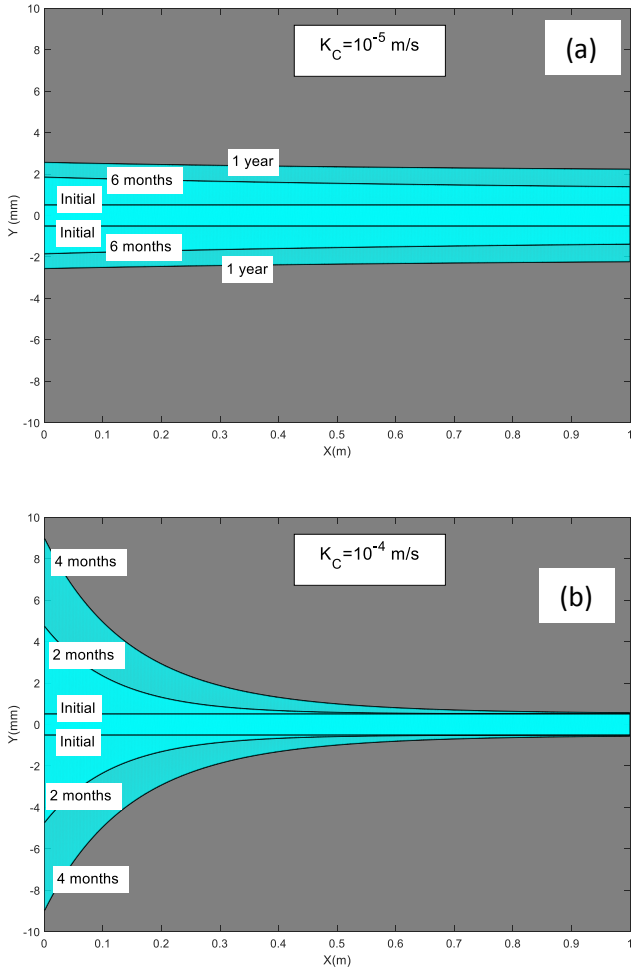

Figure 7. Fracture aperture evolution: (a) for low ($K_C = 10^{-5}$ m/s) and (b) for high ($K_C = 10^{-4}$ m/s) dissolution rates.

For the case of low dissolution, Figure 7a shows an almost uniform enlargement of the fracture both at 6 months and 1 year. In this situation, the dissolution is very slow while the fluid velocity is relatively high. Thus, the crossing fluid remains weakly contaminated (the fluid is never saturated by the dissolved species during its travel). The enlargement of the aperture (Figure 7a) is a little more pronounced near the inlet, where the concentration is zero, than near the outlet, where the fluid is slightly contaminated. Figures 8a, b and c depict, respectively the concentration, the aperture and the velocity distribution along the fracture at t = 6 months.

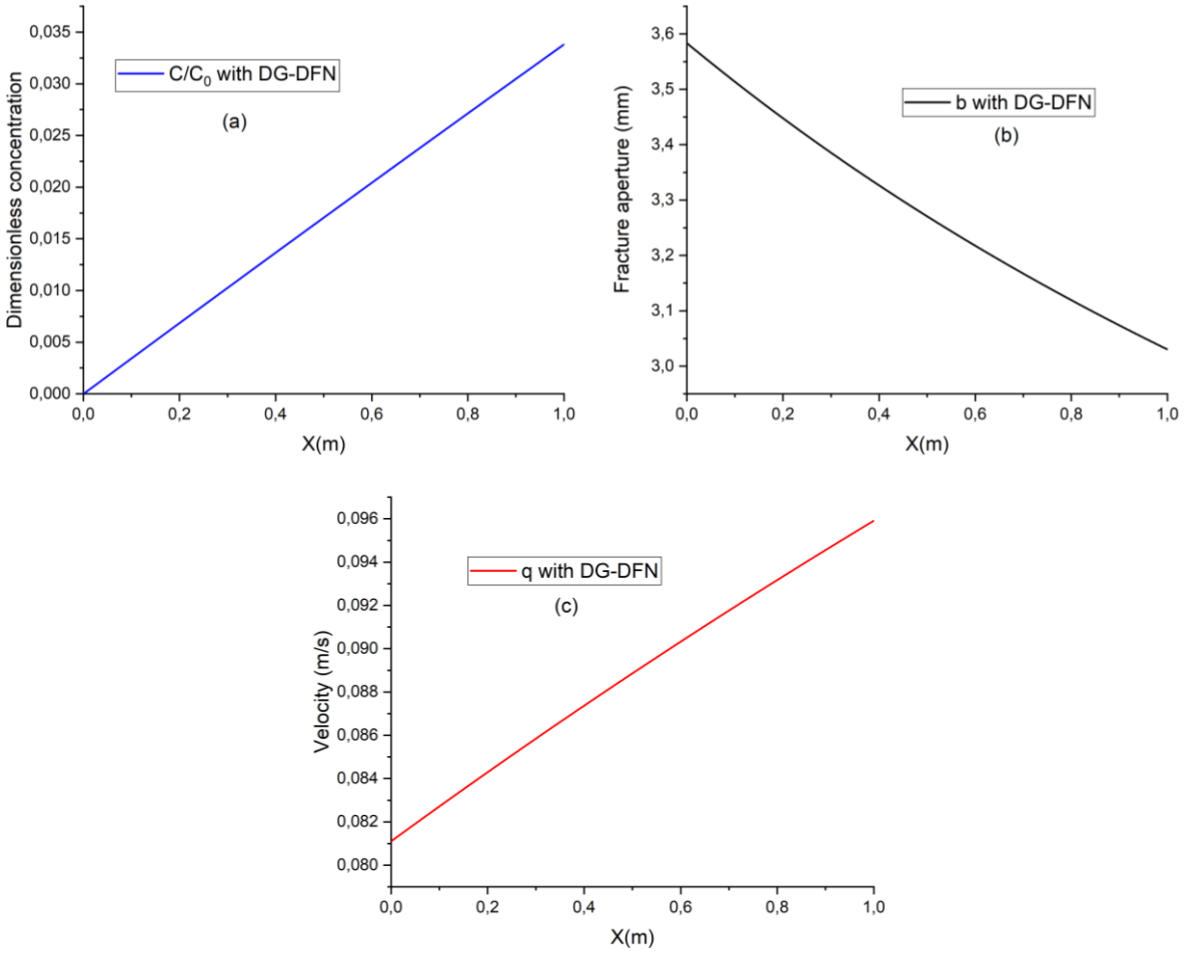

Figure 8. Dimesnionless concentration (a), aperture (b) and velocity (c) along the fracture at t = 6 months for the low dissolution case.

In Figure 8a, the concentration increases linearly inside the fracture from the left boundary, where the concentration is zero (freshwater boundary condition) to the right outlet boundary. During its travel, the fluid is contaminated by the dissolved species, which explains the linear increase of the concentration along the fracture (Figure 8a). Because of the low dissolution rate, the concentration of the fluid remains very small, reaching a maximum dimensionless concentration of only 0.035 near the outlet. Hence, the dissolved quantity along the fracture, which is proportional to $(C_S - C)$, is almost constant. Figure 8b depicts the enlargement along the fracture at t = 6 months. The aperture is around 15% more significant near the upstream (where the concentration is fixed to zero) than near the downstream. On the other hand,

because of mass conservation, a linear increase of the velocity is observed along the fracture (Figure 8c) while the aperture decreases linearly (figure 8b).

Figure 9 depicts the time evolution of the concentration, the aperture, and the velocity at the center (x=0.5m) of the fracture. The dimensionless concentration (figure 9a) decreases quickly from 1 (initially, the fluid inside the fracture is saturated by the dissolution species) to 0.4 due to fast arrival of the advection front. Then, the concentration decreases with time due to the enlargement of the fracture aperture. After 1 month, the concentration is very small, thus the rate of dissolution, which is proportional to $(C_S - C)$ is almost constant. This explains the linear increase of the fracture aperture with time, as shown in Figure 9c. The velocity inside the fracture evolves more significantly during time (Figure 9b) since it is proportional to the square of the aperture (See Eq.(2)).

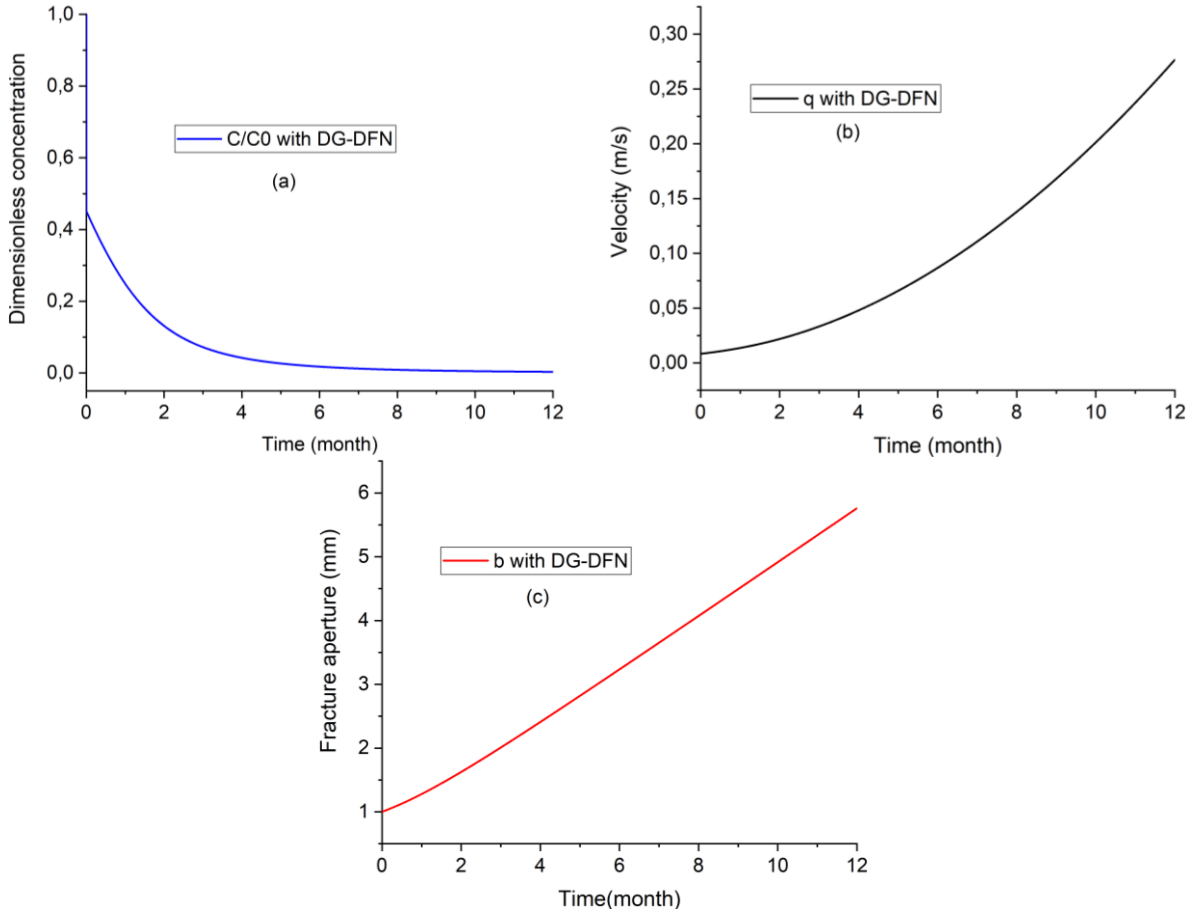

Figure 9. Time evolution of the dimensionless concentration (a), velocity (b) and aperture (c) at x=0.5m the low dissolution case.

For the case of a high dissolution rate, Figure 7b shows a funnel-shaped enlargement of the fracture with a strong increase of the aperture near the upstream, whereas the downstream remains unchanged. This result is coherent with the experimental results obtained in Li et al. 2021. Figures 10a, b and c depict, respectively the concentration, the aperture, and the velocity distribution along the fracture at t = 2months.

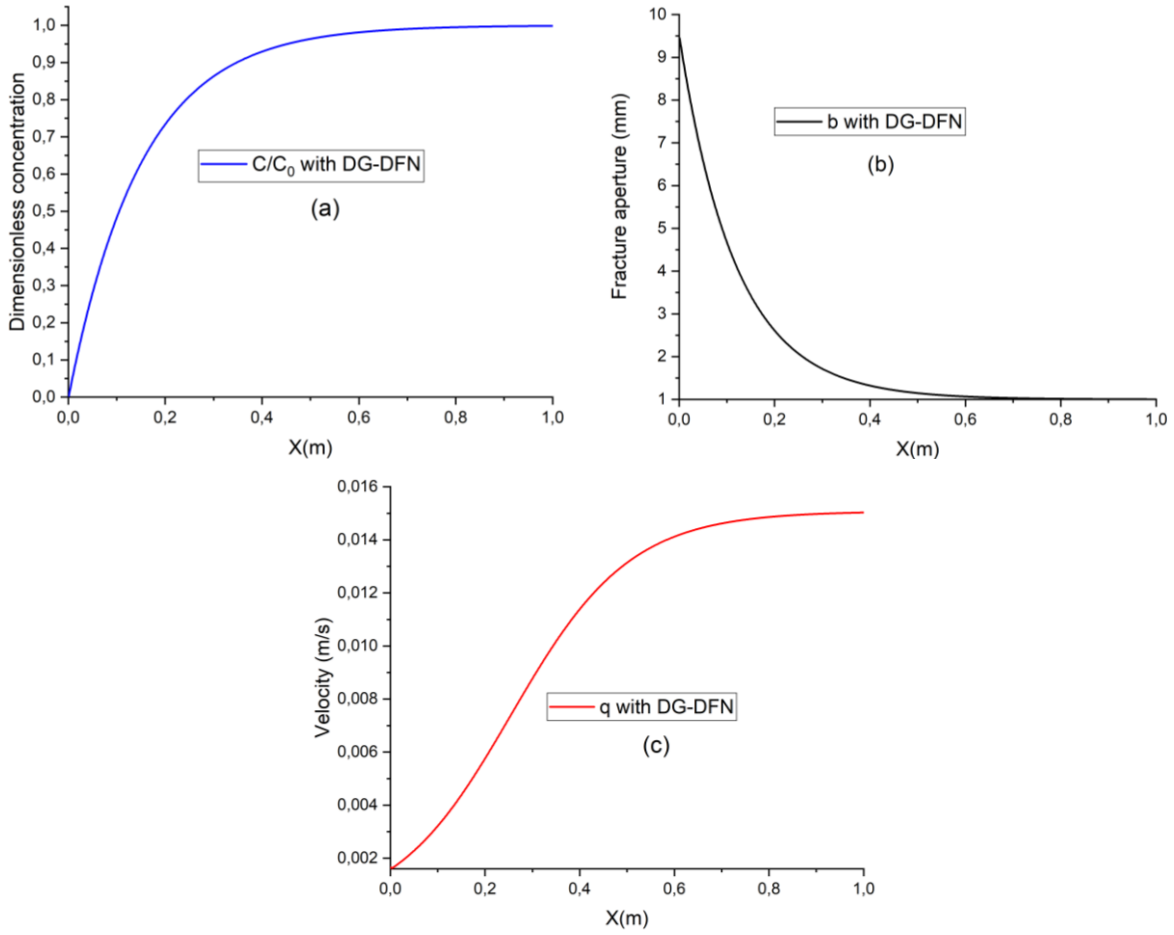

Figure 10. Dimensionless concentration (a), aperture (b) and velocity (c) along the fracture at t = 2 months for the high dissolution case.

Because of the high dissolution rate, the concentration of the fluid crossing the fracture increases significantly from zero (at the entry of the fracture) to reach 90% of Cs after only 0.3m (Figure 10a) and the fluid is almost saturated by the dissolved species at around 0.5m. As a consequence, the fracture evolution, which is proportional to $(C_S - C)$, is very high near the inlet, but quickly decreases and becomes negligible for the second half of the fracture (Figure 10b). Further, due to mass conservation, the fluid velocity along the fracture (Figure 10c) starts with a very weak value at the left (because of the high enlargement at the entry), then, it increases until around the center of the fracture (because of the decrease of the aperture) and remains almost constant for the second half of the fracture for which the aperture was unchanged.

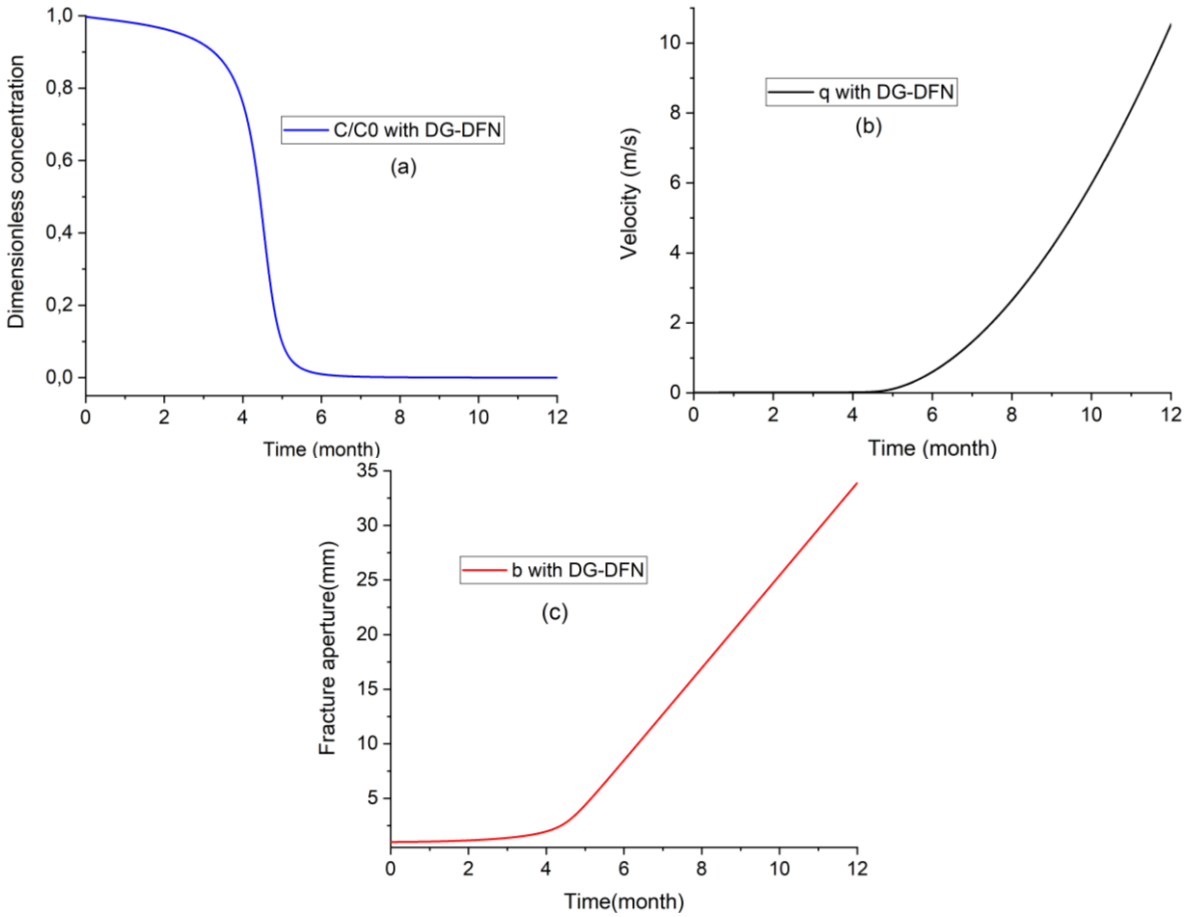

Figure 11. Time evolution of dimensionless concentration (a), velocity (b) and aperture (c) at x=0.5m for the high dissolution case.

Figure 11 depicts the time evolution of the concentration, velocity and aperture at the center of the fracture (x = 0.5m) for the high dissolution case. The velocity (Figure 11b) remains very small inside the fracture until a time $t^* \simeq 5$ months, then it starts to considerably increase with time. Indeed, during the first period ($t \leq t^*$), the funnel aperture distribution (Figure 7b) yields a permeability (proportional to the square of the aperture) distribution which is very high near the entry (large aperture), l (c) y low for the right part of the fracture with the unchanged small aperture. For such a situation (low and high permeabilities in series), the fluid velocity is mainly controlled by the low permeability. Thus, the velocity remains small until the enlargement reaches the right end of the fracture which occurs at around t^*. After that time, all the fracture enlarges (Figure 11c) and the equivalent permeability of the fracture strongly increases, yielding a highly increasing velocity (Figure 11b). As a consequence, the

concentration in the fracture (Figure 11a) strongly reduces after t^* due to the high advection flux of freshwater arriving from the left boundary.

4.2 Effect of the dissolution rate in the case of a DFN

This section extends the discussion of the previous section to a DFN. We consider a network of connected horizontal and vertical fractures, as in Figure 12.

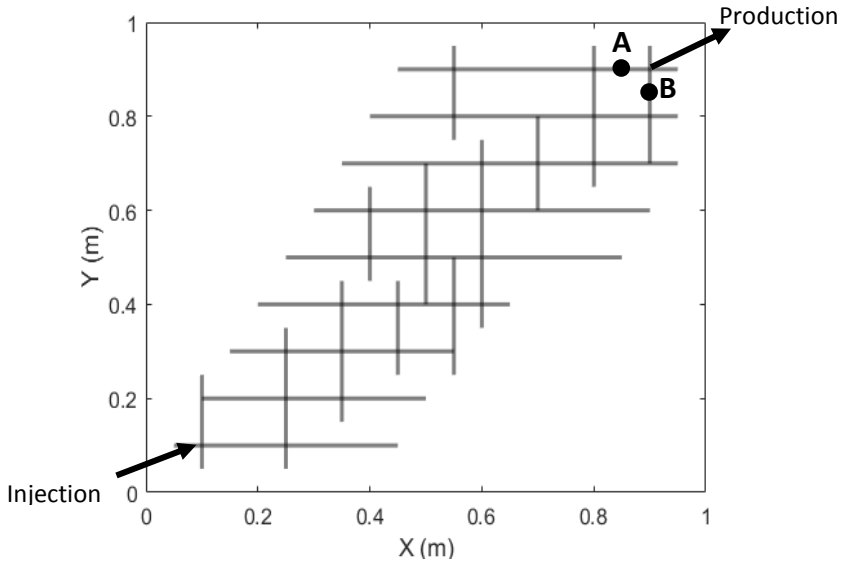

Figure 12. Conceptual model for flow, dissolution and transport in a network of fractures.

The domain is a horizontal plane, initially saturated with a solute species and as shown in the Figure 12, the freshwater is injected at the left-bottom corner. Contaminated water, due to the dissolved species, is pumped out at the right-top corner. The production rate is fixed to 10^{-4} m^2/s and is similar to the injection rate. Two dissolution values are considered, corresponding to low ($K_C = 10^{-5}$ m/s) and high ($K_C = 10^{-4}$ m/s) dissolution rates. For the rest of the input parameters, the same values are considered as in the previous case of the single fracture.

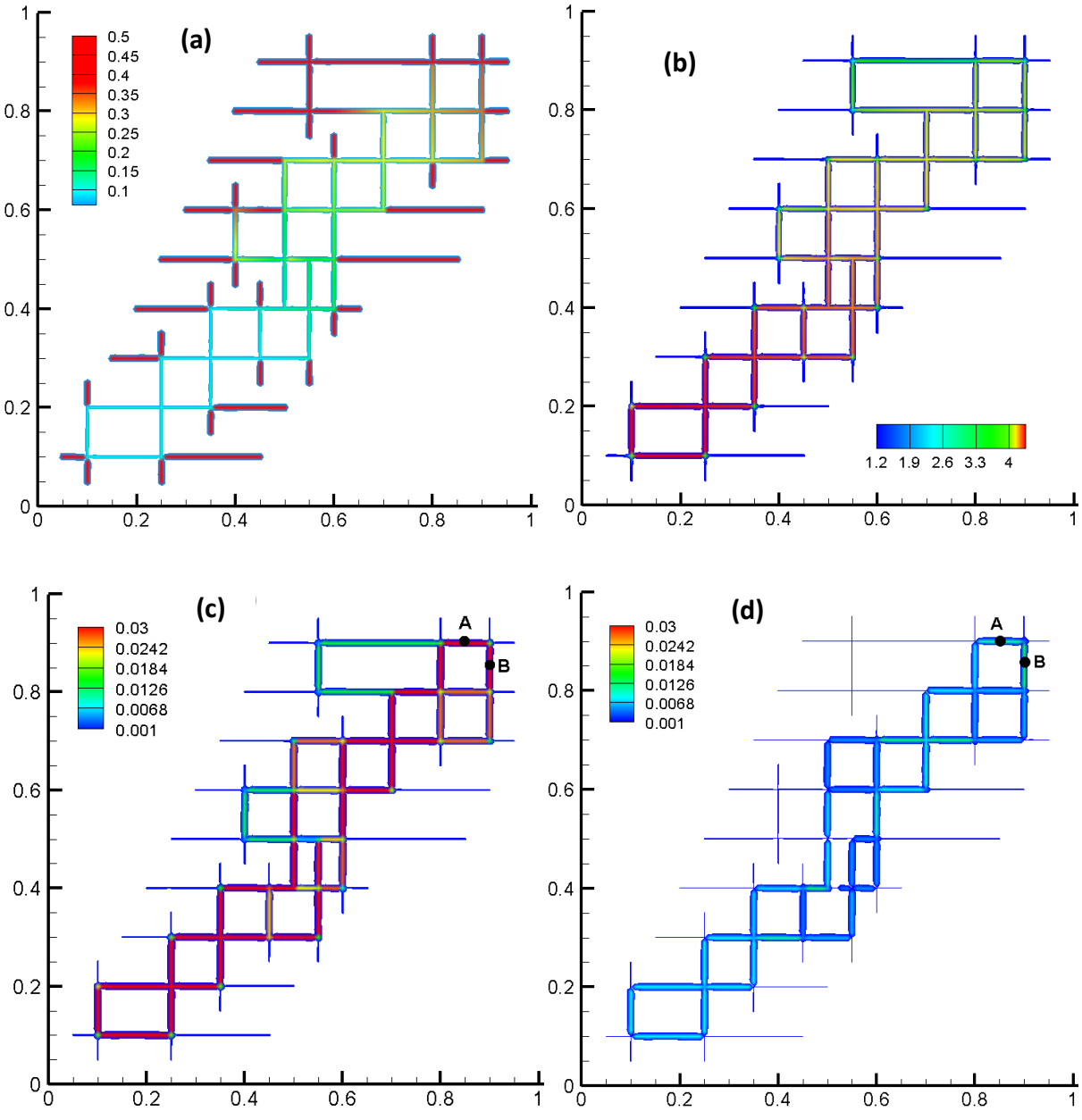

Figure 13. Results for the low dissolution rate ($K_C = 10^{-5}$ m/s): (a) distribution of the dimensionless concentration after one year, (b) aperture (mm) distribution after 1 year, (c) and (d) are the distributions of the velocity magnitude (m/s) after 100s and 1 year, respectively.

Figure 13a shows the distribution of the dimensionless concentration after one year. Initially, all fractures are filled by the dissolved specie, and no dissolution occurs. During its travel, the injected freshwater is contaminated by the dissolution process. As a consequence, the concentration inside the fractures increases from the injection well to the production well as can be observed in the Figure 13a. This figure also shows that isolated fracture branches remain contaminated by the dissolution species as the injected water cannot go through these

branches since they are plugged at their extremities. Figure 13b shows the fracture aperture distribution in the DFN after one year. Since dissolution is proportional to the difference $(C-C_S)$, the aperture is maximum near the injection well, reaching 6mm and decreases almost linearly when going to the production well in the vicinity of which it reaches 4mm. This uniform decrease is almost similar to the one observed for the single fracture in the case of the small dissolution rate (Figure 7a). Figure 13c and 13d show the velocity distribution, respectively, after 100s and 1 year. At t=100s, the velocity is almost significant in all connected fractures (it is zero for plugged fractures). Due to the enlargement of fractures aperture, the velocity inside the fractures decreases with time as can be observed after 1 year in Figure 13d. Note that this phenomenon has not been observed for the single fracture for which we obtained an increase of the velocity with time for both low (Figure 9b) and high (figure 11b) dissolution rates. The difference between the previous single fracture configuration and the current DFN configuration is due to the difference of the boundary conditions between these two configurations. Indeed, for the single fracture, we had fixed hydraulic heads in upstream and downstream. Thus, the total flow rate crossing the fracture, is controlled by the difference between the upstream and downstream heads as well as by the permeability of the fracture. The enlargement of the fracture, due to dissolution, induces a significant increase of the flow rate because of the increase of the permeability, which is proportional to the square of the aperture. Hence, due to dissolution, the velocity inside the fractures increases with time (see Figures 9b and 11b). For the current DFN configuration, the total flow rate is fixed and corresponds to the injected flow rate. Thus, dissolution induces an enlargement of the fracture aperture, which induces a decrease in the velocity because of mass conservation principle. Note that for the DFN configuration, although the total flow rate is fixed, the flow rate inside each fracture varies with time since the distribution of the aperture of fracture branches can vary due to dissolution. As a consequence, during simulation, the

distribution of the permeability in the DFN can vary, which can induce a modification of the flowrate repartition between the fractures. For instance, Figure 14 shows the aperture, velocity and flow rate evolution for the two last fractures A and B in the vicinity of the pumping well (see location in Figure 12). For both fractures A and B, the aperture increases linearly with time (Figures 14a and 14d). The velocity inside the two fractures decreases with time (Figures 14b and 14e). The flow rate inside the two fractures is not constant and has a different monotonic behavior during time. The flow rate decreases with time in the fracture A (Figure 14c), whereas it increases in the fracture B (Figure 14f). The sum of the two flowrates in the fractures A and B is constant and is equal to the pumped flowrate since A and B are the only non-plugged fractures connected to the pumping well.

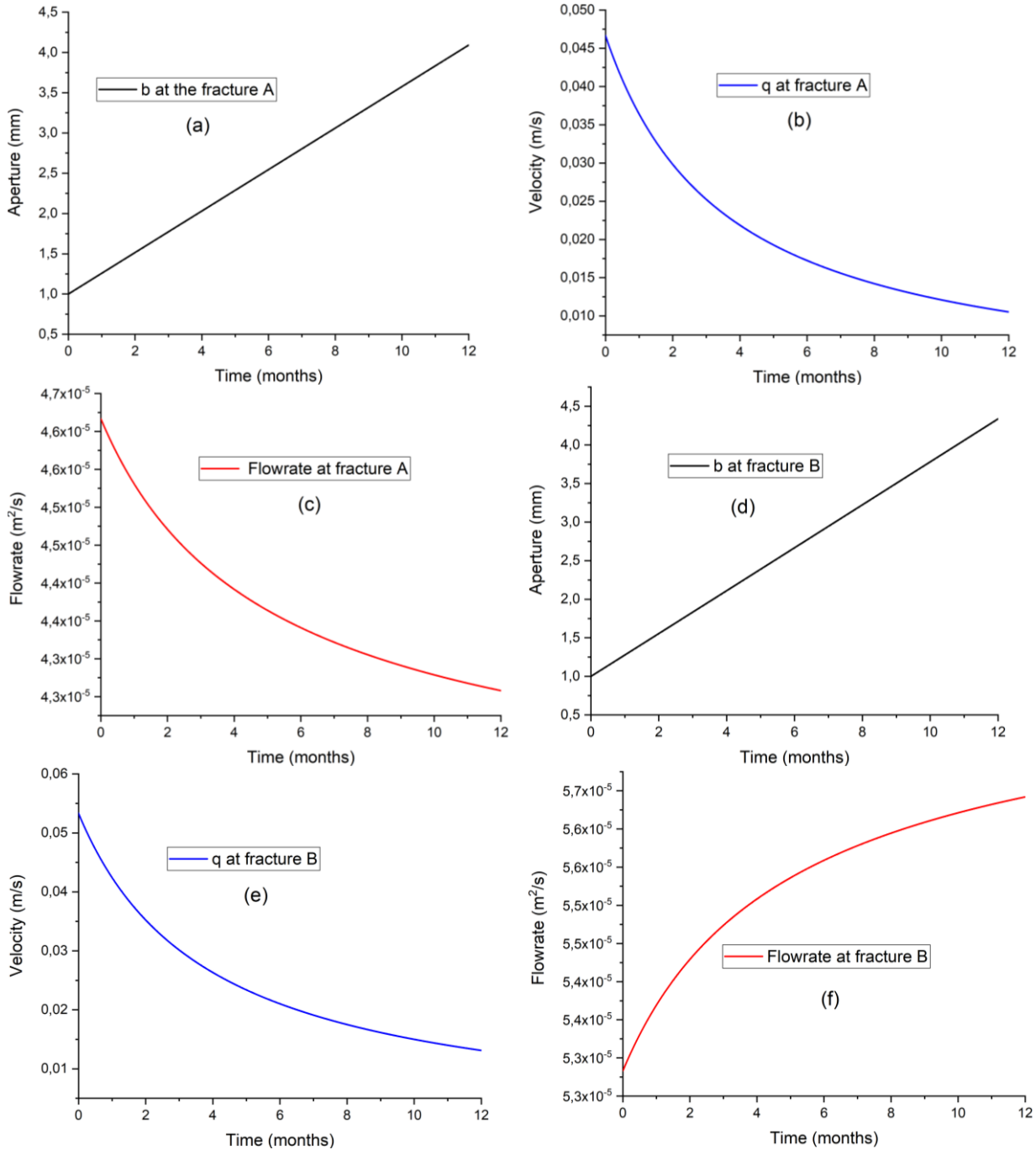

Figure 14. Aperture (a), velocity (b) and flowrate (c) evolutions in the fracture A and aperture (d), velocity (e) and flow rate (f) evolutions in the fracture B for the low dissolution case ($K_C = 10^{-5}$ m/s).

Figure 15 shows the concentration, aperture and velocity distribution in the case of high dissolution ($K_C = 10^{-4}$ m/s). After one year, the concentration reduces only near the injection well (Figure 15a). Indeed, due to the high dissolution rate, during its travel, the fluid becomes quickly saturated by the dissolution species. As in the single fracture configuration (Figure 7b), a very high enlargement is observed near the injection well, with an aperture reaching a value of 50 mm, whereas the aperture remains almost at its initial value near the pumping well (Figure 15b). The velocity distribution after 100s shows a high velocity for almost all connected fractures (Figure 15c), whereas after 1 year, it has strongly reduced (due to the high enlargement) near the injection point and remains high close to the pumping well (Figure 15d).

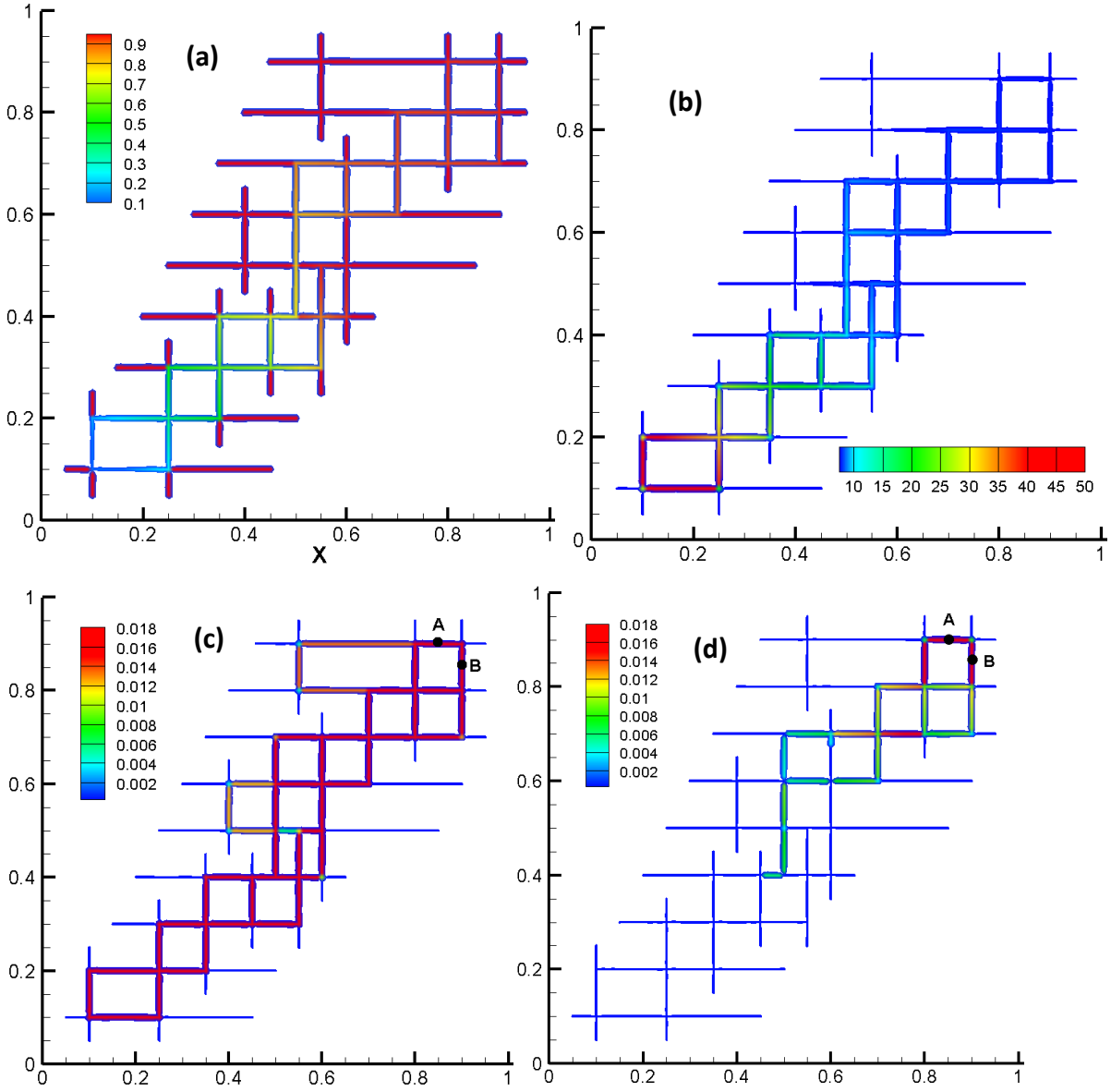

Figure 15: Results for the high dissolution rate ($K_C = 10^{-4}$ m/s): Distribution of the dimensionless concentration (-) (a) and aperture (mm) (b) after 1 year and magnitude of the velocity (m/s) after 100s (c) and 1 year (d).

Figure 16 depicts the evolution of aperture, velocity and flow rate in the two fractures A and B, sharing the pumping well for the high dissolution case. For both fractures A and B, the aperture (Figures 16a and 16d) shows an almost slight linear evolution with time which is less significant than for the low dissolution case (Figure 14). According to this aperture increase, the velocity in both fractures shows an almost linear decrease with time (Figures 16b and 16e). However, contrarily to the low dissolution case, the flow rate in the two fractures shows a non-monotonic evolution with time (Figures 16c and 16e). Indeed, the flow rate in the

fracture A shows a decrease until around 5 months and an increase after that, whereas the flow rate in the fracture B depicts the opposite behavior, thus the sum of the two flow rates remains constant. This parabolic evolution of the flow rate is probably related to the change of the permeability distribution during the simulation due to dissolution in the DFN.

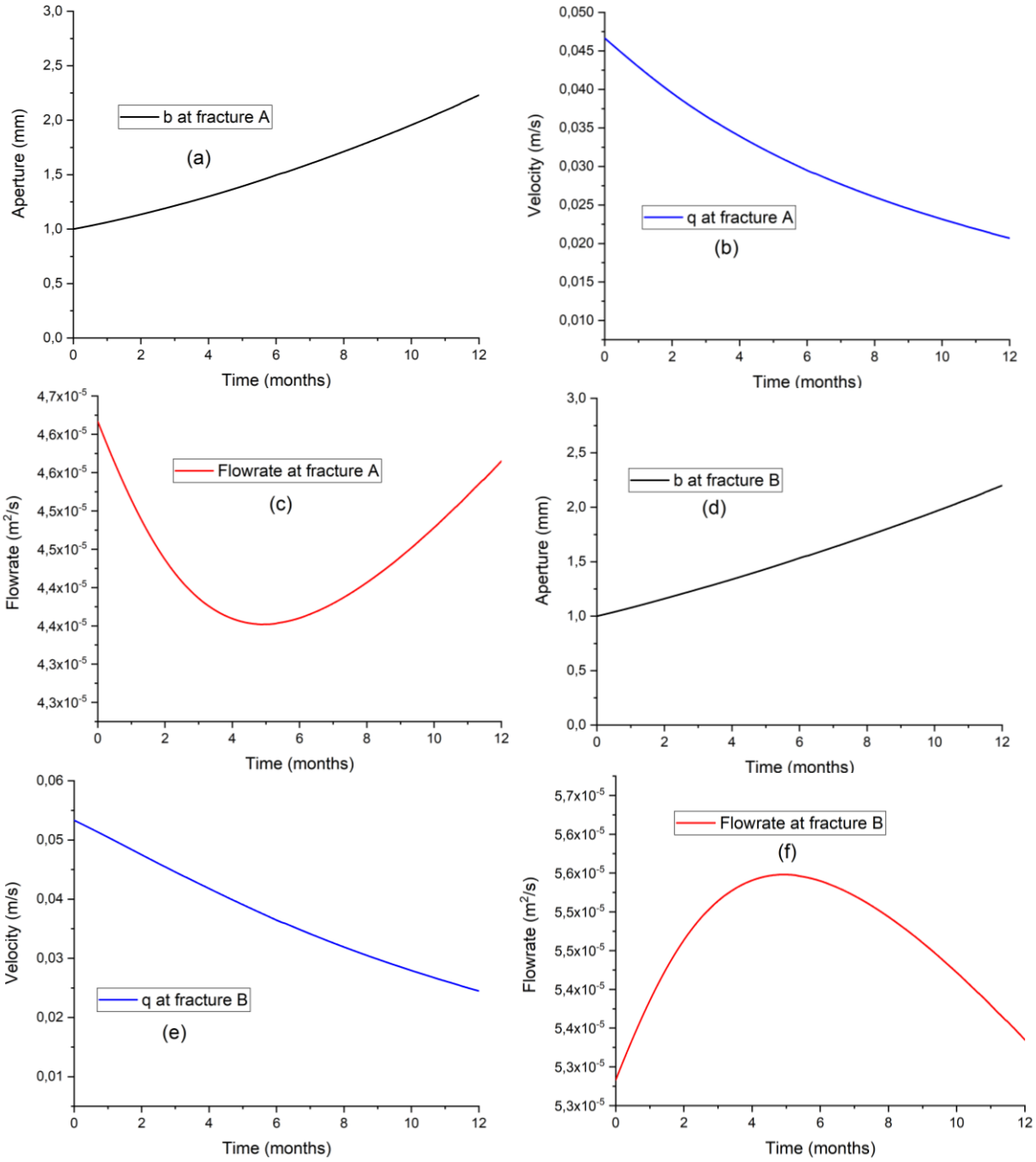

Figure 16: Aperture (a), velocity (b) and flowrate (c) evolutions in the fracture A and aperture (d), velocity (e) and flowrate (f) evolutions in the fracture B for the high dissolution rate ($K_C = 10^{-4}$ m/s).

6. Conclusion

Modeling dissolution processes in a DFN is a computationally challenging problem because of the nonlinear coupling between flow, transport and reactive processes, introduced by the impact of dissolution on the fracture aperture. The challenge is accentuated by the fact that in the fractures, the transport is advection dominated. In such a case, standard FE formulations introduce unphysical oscillations that can lead to convergence issues. The upwind FV formulation give stable results but introduces a large amount of numerical diffusion. In this work, we developed a new model based on advanced numerical schemes to simulate dissolution processes in DFNs. The model is based on coupling the MFE method for flow with the DG scheme for transport. The DG method is known to be suitable for advection-dominated problems, as it avoids unphysical oscillations and reduces numerical diffusion. A new formulation of the DG was proposed for the Riemann solver at the intersection of fractures. The newly developed scheme calculates the upstream concentration based on the average of the nodal concentration of all fractures having an inflow at the intersection node, weighted by the water fluxes through these fractures. The dispersion term is calculated with the MFE method which allows to ensure the continuity of the dispersive flux at the intersection of several fractures having different apertures. The time integration of the obtained nonlinear coupled flow-transport-dissolution equations is improved by using an advanced solver of ODEs via the MOL.

The developed DG model is first verified for linear transport in a DFN by comparison against a standard FE solution obtained with COMSOL Multiphysics and an upwind FV model. Good agreement is obtained between the three models in the case of high diffusion. For advection-dominated transport configurations, often encountered because of the rapid flow in fractures, the DG-DFN model avoids the unphysical oscillations observed with FE results and allows for capturing sharp concentration fronts with a relatively coarse mesh. The upwind FV

method fails to capture these fronts because of numerical diffusion, but its solution converges towards the DG solution when a very fine mesh is employed.

The new DG model was then verified in the case of coupled flow, transport and aperture evolution due to dissolution for a single fracture. Although, we have used a high diffusion value, the FE solution showed numerical oscillations at short times near the outlet. The overall long-term results of FE, FV and DG models are in very good agreement in terms of concentration distribution and aperture evolution.

The new DG model was then used to investigate the effect of the dissolution rate on flow, transport and aperture evolutions in the case of a single fracture and in the case of a DFN. In the case of low dissolution, the fluid remains weakly contaminated (the fluid is never saturated by the dissolved species during its travel). A linear increase of the fracture aperture with time is observed. The velocity inside the fractures increases over time because of the increase of permeability (proportional to the square of the aperture) in the case of flow induced by fixed hydraulic heads at the upstream and downstream boundaries. In the case where the total flow rate is fixed, the velocity inside fractures decreases when the aperture increases due to dissolution, because of fluid mass conservation.

In the case of a high dissolution rate, the fluid becomes quickly saturated by the dissolution species during its travel. As a consequence, a very high enlargement is observed near the injection, whereas the aperture remains almost at its initial value away from the injection. The velocity is strongly reduced (due to the high enlargement) near the injection point and remains high away from the injection.

In the case of a DFN, although the total flow rate is fixed, the flowrate through each fracture can vary with time since the distribution of the permeability of the fractures can vary with time because of dissolution, which can induce a variation of the flowrate repartition between

the fractures. For the case of a low dissolution rate, we observed a monotonic evolution of the flow rate inside fractures, whereas, in the case of a high dissolution rate, we observed a parabolic evolution of the flowrate through fractures, related to the change of the permeability distribution during the simulation due to the dissolution in the DFN.

The model considered in this study is limited to dissolution processes, but the numerical scheme can be generalized to dissolution/precipitation processes. Precipitation processes may occur and could be important under non isothermal conditions. Thus, a future extension of this work could be including precipitation and thermal processes.

References

Aliouache, Mohammed, Xiaoguang Wang, Hervé Jourde, Zhaoqin Huang, and Jun Yao. "Incipient Karst Formation in Carbonate Rocks: Influence of Fracture Network Topology." *Journal of Hydrology* 575 (August 2019): 824–37. https://doi.org/10.1016/j.jhydrol.2019.05.082.

Ameli, Pasha, Jean E. Elkhoury, Joseph P. Morris, and Russell L. Detwiler. "Fracture Permeability Alteration Due to Chemical and Mechanical Processes: A Coupled High-Resolution Model." *Rock Mechanics and Rock Engineering* 47, no. 5 (September 2014): 1563–73. https://doi.org/10.1007/s00603-014-0575-z.

Barton, Colleen A., and Mark D. Zoback. "Self-Similar Distribution and Properties of Macroscopic Fractures at Depth in Crystalline Rock in the Cajon Pass Scientific Drill Hole." *Journal of Geophysical Research* 97, no. B4 (1992): 5181. https://doi.org/10.1029/91JB01674.

Brown, Peter N., Alan C. Hindmarsh, and Linda R. Petzold. "Using Krylov Methods in the Solution of Large-Scale Differential-Algebraic Systems." *SIAM Journal on Scientific Computing* 15, no. 6 (November 1994): 1467–88. https://doi.org/10.1137/0915088.

Deng, Hang, and Nicolas Spycher. "Modeling Reactive Transport Processes in Fractures." *Reviews in Mineralogy and Geochemistry* 85, no. 1 (September 1, 2019): 49–74. https://doi.org/10.2138/rmg.2019.85.3.

Detwiler, Russell L., Robert J. Glass, and William L. Bourcier. "Experimental Observations of Fracture Dissolution: The Role of Peclet Number on Evolving Aperture Variability: FRACTURE DISSOLUTION." *Geophysical Research Letters* 30, no. 12 (June 2003). https://doi.org/10.1029/2003GL017396.

Detwiler, Russell L., and Harihar Rajaram. "Predicting Dissolution Patterns in Variable Aperture Fractures: Evaluation of an Enhanced Depth-Averaged Computational Model" *Water Resources Research* 43, no. 4 (April 2007). https://doi.org/10.1029/2006WR005147.

Dijk, Peter Erik, Brian Berkowitz, and Yoseph Yechieli. "Measurement and Analysis of Dissolution Patterns in Rock Fractures" *Water Resources Research* 38, no. 2 (February 2002): 5-1-5–12. https://doi.org/10.1029/2001WR000246.

Fahs, Marwan, Anis Younes, and François Lehmann. "An Easy and Efficient Combination of the Mixed Finite Element Method and the Method of Lines for the Resolution of Richards' Equation." *Environmental Modelling & Software* 24, no. 9 (September 2009): 1122–26. https://doi.org/10.1016/j.envsoft.2009.02.010.

Farthing, Matthew W, Christopher E Kees, and Cass T Miller. "Mixed Finite Element Methods and Higher Order Temporal Approximations for Variably Saturated Groundwater Flow." *Advances in Water Resources* 26, no. 4 (2003): 373–94.

Graf, T., Therrien, R., 2007. Coupled thermohaline groundwater flow and single-species reactive solute transport in fractured porous media. Advances in Water Resources 30, 742–771. https://doi.org/10.1016/j.advwatres.2006.07.001

Hanna, R. Blair, and Harihar Rajaram. “Influence of Aperture Variability on Dissolutional Growth of Fissures in Karst Formations.” *Water Resources Research* 34, no. 11 (November 1998): 2843–53. https://doi.org/10.1029/98WR01528.

Hayek, Mohamed, Georg Kosakowski, Andreas Jakob, and Sergey V. Churakov. “A Class of Analytical Solutions for Multidimensional Multispecies Diffusive Transport Coupled with Precipitation-Dissolution Reactions and Porosity Changes.” *Water Resources Research* 48, no. 3 (March 2012). https://doi.org/10.1029/2011WR011663.

He, X., Sinan, M., Kwak, H., Hoteit, H., 2021. A corrected cubic law for single-phase laminar flow through rough-walled fractures. Advances in Water Resources 154, 103984. https://doi.org/10.1016/j.advwatres.2021.103984

Hooker, J.N., J.F.W. Gale, L.A. Gomez, S.E. Laubach, R. Marrett, and R.M. Reed. “Aperture-Size Scaling Variations in a Low-Strain Opening-Mode Fracture Set, Cozzette Sandstone, Colorado.” *Journal of Structural Geology* 31, no. 7 (July 1, 2009): 707–18. https://doi.org/10.1016/j.jsg.2009.04.001.

Hosseini, N., Bajalan, Z., Khoei, A.R., 2020. Numerical modeling of density-driven solute transport in fractured porous media with the extended finite element method. Advances in Water Resources 136, 103453. https://doi.org/10.1016/j.advwatres.2019.103453

Khoei, A.R., Salehi Sichani, A., Hosseini, N., 2020. Modeling of reactive acid transport in fractured porous media with the Extended–FEM based on Darcy-Brinkman-Forchheimer framework. Computers and Geotechnics 128, 103778. https://doi.org/10.1016/j.compgeo.2020.103778

Kim, Jihoon, Eric Sonnenthal, and Jonny Rutqvist. “A Sequential Implicit Algorithm of Chemo-Thermo-Poro-Mechanics for Fractured Geothermal Reservoirs.” *Computers & Geosciences* 76 (March 2015): 59–71. https://doi.org/10.1016/j.cageo.2014.11.009.

Konz, M., P. Ackerer, A. Younes, P. Huggenberger and E. Zechner. Two-dimensional stable-layered laboratory-scale experiments for testing density-coupled flow models. Water Resources Research 45, Issue2, (2009), https://doi.org/10.1029/2008WR007118

Koohbor, B., M. Fahs, H. Hoteit, J. Doummar, A. Younes, and B. Belfort. “An Advanced Discrete Fracture Model for Variably Saturated Flow in Fractured Porous Media.” *Advances in Water Resources* 140 (June 2020): 103602. https://doi.org/10.1016/j.advwatres.2020.103602.

Li, W., Germaine, J.T., Einstein, H.H., 2021. Transport- Controlled Dissolution in an Evolving Fracture: The Extended Purday Solution and Fracture Flow Tests. Water Resources Research 57. https://doi.org/10.1029/2020WR029166

Liu, Min, Vitalii Starchenko, Lawrence M. Anovitz, and Andrew G. Stack. “Grain Detachment and Transport Clogging during Mineral Dissolution in Carbonate Rocks with Permeable Grain Boundaries.” *Geochimica et Cosmochimica Acta* 280 (July 2020): 202–20. https://doi.org/10.1016/j.gca.2020.04.022.

Lopes, Juliana A.G., Walter E. Medeiros, Vincenzo La Bruna, Alexandre de Lima, Francisco H.R. Bezerra, and Denis José Schiozer. “Advancements towards DFKN Modelling: Incorporating Fracture Enlargement Resulting from Karstic Dissolution in Discrete Fracture Networks.” *Journal of Petroleum Science and Engineering* 209 (February 2022): 109944. https://doi.org/10.1016/j.petrol.2021.109944.

Medekenova, Alfiya, and Gareth D. Jones. “Characterization and Modeling Challenges Associated with Fracture and Karst (Non-Matrix) in the Margin Area of a Carbonate

Reservoir." In *All Days*, SPE-172275-MS. Astana, Kazakhstan: SPE, 2014. https://doi.org/10.2118/172275-MS.

Medici, G., L.J. West, and N.P. Mountney. "Characterizing Flow Pathways in a Sandstone Aquifer: Tectonic vs Sedimentary Heterogeneities." *Journal of Contaminant Hydrology* 194 (November 2016): 36–58. https://doi.org/10.1016/j.jconhyd.2016.09.008.

Miller, Cass T, Chandra Abhishek, and Matthew W Farthing. "A Spatially and Temporally Adaptive Solution of Richards' Equation." *Advances in Water Resources* 29, no. 4 (2006): 525–45.

Moortgat, Joachim, Mohammad Amin Amooie, and Mohamad Reza Soltanian. "Implicit Finite Volume and Discontinuous Galerkin Methods for Multicomponent Flow in Unstructured 3D Fractured Porous Media." *Advances in Water Resources* 96 (October 2016): 389–404. https://doi.org/10.1016/j.advwatres.2016.08.007.

Mukhametdinova, Aliya, Andrey Kazak, Tagir Karamov, Natalia Bogdanovich, Maksim Serkin, Sergey Melekhin, and Alexey Cheremisin. "Reservoir Properties of Low-Permeable Carbonate Rocks: Experimental Features." *Energies* 13, no. 9 (May 3, 2020): 2233. https://doi.org/10.3390/en13092233.

Natarajan, N, and G Suresh Kumar. "Solute Transport in a Coupled Fracture-Matrix System with Sinusoidal Fracture Geometry." *International Journal of Engineering Science and Technology* 2, no. 6 (2010): 1886–1992.

Sahu, Q., Fahs, M., Hoteit, H., 2023. Optimization and Uncertainty Quantification Method for Reservoir Stimulation through Carbonate Acidizing. ACS Omega 8, 539–554. https://doi.org/10.1021/acsomega.2c05564

Steefel, C.I., Lasaga, A.C., 1994. A coupled model for transport of multiple chemical species and kinetic precipitation/dissolution reactions with application to reactive flow in single phase hydrothermal systems. American Journal of Science 294, 529–592. https://doi.org/10.2475/ajs.294.5.529

Steefel, C.I., Lichtner, P.C., 1998. Multicomponent reactive transport in discrete fractures. Journal of Hydrology 209, 200–224. https://doi.org/10.1016/S0022-1694(98)00173-5

Suk, Heejun. "Generalized Semi-Analytical Solutions to Multispecies Transport Equation Coupled with Sequential First-Order Reaction Network with Spatially or Temporally Variable Transport and Decay Coefficients." *Advances in Water Resources* 94 (August 2016): 412–23. https://doi.org/10.1016/j.advwatres.2016.06.004.

Tenthorey, E, and J Fitzgerald. "Feedbacks between Deformation, Hydrothermal Reaction and Permeability Evolution in the Crust: Experimental Insights." *Earth and Planetary Science Letters* 247, no. 1–2 (July 15, 2006): 117–29. https://doi.org/10.1016/j.epsl.2006.05.005.

Tran, Minh, and Birendra Jha. "Effect of Poroelastic Coupling and Fracture Dynamics on Solute Transport and Geomechanical Stability." *Water Resources Research* 57, no. 10 (October 2021). https://doi.org/10.1029/2021WR029584.

Viswanathan, H. S., J. Ajo- Franklin, J. T. Birkholzer, J. W. Carey, Y. Guglielmi, J. D. Hyman, S. Karra, et al. "From Fluid Flow to Coupled Processes in Fractured Rock: Recent Advances and New Frontiers." *Reviews of Geophysics* 60, no. 1 (March 2022). https://doi.org/10.1029/2021RG000744.

Witherspoon, P.A., J.S.Y. Wang, K. Iwai, J.E. Gale, Validity of Cubic Law for fluid flow in a deformable rock fracture, Water Resour. Res. 16 (1980) 1016–1024. https://doi.org/10.1029/WR016i006p01016.

Younes, A., M. Konz, M. Fahs, A. Zidane, and P. Huggenberger. "Modelling Variable Density Flow Problems in Heterogeneous Porous Media Using the Method of Lines and Advanced Spatial Discretization Methods." *Mathematics and Computers in Simulation* 81, no. 10 (June 2011): 2346–55. https://doi.org/10.1016/j.matcom.2011.02.010.

Younes, Anis, and Philippe Ackerer. "Solving the Advection-Dispersion Equation with Discontinuous Galerkin and Multipoint Flux Approximation Methods on Unstructured Meshes." *International Journal for Numerical Methods in Fluids* 58, no. 6 (October 30, 2008): 687–708. https://doi.org/10.1002/fld.1783.

Younes, Anis, Marwan Fahs, and Selim Ahmed. "Solving Density Driven Flow Problems with Efficient Spatial Discretizations and Higher-Order Time Integration Methods." *Advances in Water Resources* 32, no. 3 (March 2009): 340–52. https://doi.org/10.1016/j.advwatres.2008.11.003.

Younes, Anis, Ahmed Makradi, Ali Zidane, Qian Shao, and Lyazid Bouhala. "A Combination of Crouzeix-Raviart, Discontinuous Galerkin and MPFA Methods for Buoyancy-Driven Flows." *International Journal of Numerical Methods for Heat & Fluid Flow* 24, no. 3 (April 1, 2014): 735–59. https://doi.org/10.1108/HFF-07-2012-0156.

Younes, A., Koohbor, B., Fahs, M., Hoteit, H., 2023. An efficient discontinuous Galerkin - mixed finite element model for variable density flow in fractured porous media. Journal of Computational Physics 477, 111937. https://doi.org/10.1016/j.jcp.2023.111937

Zidane, Ali, and Abbas Firoozabadi. "An Efficient Numerical Model for Multicomponent Compressible Flow in Fractured Porous Media." *Advances in Water Resources* 74 (December 2014): 127–47. https://doi.org/10.1016/j.advwatres.2014.08.010.